

# The clustering and luminosity function of quasars in the FLAMINGO simulation

**MSc thesis**

Boyi Ding



Universiteit  
Leiden  
Observatory

# The clustering and luminosity function of quasars in the FLAMINGO simulation

A thesis submitted in partial fulfillment  
of the requirements for the degree of

Master of Science  
in  
Astronomy

Author:  
Student ID:  
Supervisor:  
Second supervisor:  
Daily supervisor:  
Corrector:  
Project duration:

Boyi Ding  
s3965546  
Prof. Joseph Hennawi  
Prof. Joop Schaye  
Elia Pizzati  
Prof. Joop Schaye  
Oct 2023 – July 2024

Cover image:  
Template style:  
Template licence:

Night sky by Evgeni Tcherkasski  
Thesis style by Richelle F. van Capelleveen  
Licenced under CC BY-NC-SA 4.0



Universiteit  
**Leiden**  
Observatory

P.O. Box 9513, 2300 RA Leiden, The Netherlands

# Abstract

Cosmological hydrodynamical simulations follow the non-linear evolution of structures in the Universe by modeling a large variety of processes that are important to the physics of galaxies, stars, and black holes. In the last decade, these simulations have become capable of reproducing a large number of observed galaxy properties, and started to play a key role in shaping our understanding of the formation and evolution of galaxies in the universe, as well as the relation between galaxies and the supermassive black holes (SMBHs) that are harbored at their center. While much effort has been devoted to the study of the connection between SMBHs and their hosting galaxies in terms of gas fueling and AGN feedback, only a few studies have focused on the global properties of SMBHs and their evolution over cosmic time. Specifically, SMBHs are visible at cosmological distances when they turn into bright quasars. Quasars are, however, extremely rare objects, and hence their statistical properties (such as their luminosity and spatial distributions) can only be studied theoretically when large simulated volumes are available. In this project, we use the cosmological simulations from the FLAMINGO suite (which are the largest ever run) to reproduce two basic observational probes of quasar activity: the quasar luminosity function and the quasar autocorrelation function. We study how well FLAMINGO can match observational constraints on these quantities at different redshifts. We investigate which black holes contribute to the bright quasar population, and split their relative contribution in terms of black hole mass, host halo mass, and Eddington ratio.

# Acknowledgements

## Acknowledgements

I am profoundly grateful for the opportunity to pursue my first year project at Leiden Observatory. The program has provided me with invaluable resources and a supportive environment that were instrumental in the completion of this project. I extend my deepest thanks to Prof. Joseph Hennawi, whose guidance as my supervisor has been indispensable. His encouragement to showcase my work and his insightful ideas, especially during challenging phases of my research, have significantly enriched my academic experience.

I would also like to express my gratitude to Prof. Joop Schaye for his expert guidance on issues related to the FLAMINGO project. Attending meetings with his group sparked many ideas and greatly contributed to my research development. Additionally, my daily supervisor, Elia Pizzati, deserves a special mention for his mentorship. He has patiently taught me numerous aspects of our field, always taking the time to answer my questions thoroughly and ensuring that I grew from a novice to a more confident researcher.

I wish all my mentors and Leiden Observatory a bright and successful future. Thank you for making my journey not only possible but also truly memorable.

# Contents

<b>Abstract</b> .....	<b>iv</b>
<b>Acknowledgements</b> .....	<b>v</b>
<b>List of Tables</b> .....	<b>viii</b>
<b>List of Figures</b> .....	<b>ix</b>
<b>1</b> <b>Introduction</b> .....	<b>1</b>
<b>1.1</b> <b>Quasars and Supermassive Black Holes</b>	<b>1</b>
1.1.1 Black holes and Supermassive Black Holes .....	1
1.1.2 AGN .....	1
1.1.3 Quasars and Supermassive black holes .....	2
<b>1.2</b> <b>Cosmological simulation</b>	<b>4</b>
<b>1.3</b> <b>Subgrid Model</b>	<b>5</b>
1.3.1 SMBH seeding and growth .....	6
1.3.2 AGN Feedback processes .....	7
<b>2</b> <b>Simulation</b> .....	<b>9</b>
<b>2.1</b> <b>FLAMINGO</b>	<b>9</b>
<b>3</b> <b>Methods</b> .....	<b>14</b>
<b>3.1</b> <b>Quasar Luminosity Function (QLF)</b>	<b>14</b>
<b>3.2</b> <b>Quasar clustering</b>	<b>16</b>
<b>3.3</b> <b>Eddington Radio</b>	<b>17</b>
<b>4</b> <b>Results</b> .....	<b>18</b>
<b>4.1</b> <b>Quasar Luminosity Function</b>	<b>18</b>
<b>4.2</b> <b>Cumulative Quasar Luminosity Function</b>	<b>18</b>

<b>4.3</b>	<b>Quasar Clustering</b>	<b>21</b>
<b>5</b>	<b>Discussion</b>	<b>23</b>
<b>5.1</b>	<b>Quasar Luminosity Function</b>	<b>23</b>
<b>5.2</b>	<b>Variations of the simulation</b>	<b>26</b>
5.2.1	Box sizes and Resolutions .....	26
5.2.2	Cosmological Variations .....	28
5.2.3	Astrophysical Variations .....	31
<b>5.3</b>	<b>Correlation length</b>	<b>31</b>
<b>6</b>	<b>Conclusion</b>	<b>34</b>
<b>A</b>	<b>Appendix</b>	<b>36</b>
<b>A.1</b>	<b>Eddington ratio distribution function</b>	<b>36</b>
<b>A.2</b>	<b>QLFs in bins of <math>M_{\mathrm{dm}}</math></b>	<b>36</b>
	<b>Bibliography</b>	<b>40</b>

# List of Tables

<b>2.1</b>	Comological parameters in different simulations. The values from left to right are: The dimensionless Hubble constant $h$ ; the total matter density parameter $\Omega_m$ ; the dark energy density parameter $\Omega_\Lambda$ ; the total baryonic matter density parameter $\Omega_b$ ; the combined particle mass of all neutrino species $\sum m_\nu$ ; the amplitude of the primordial matter power spectrum $A_s$ , the primordial matter power spectral index $n_s$ ; the amplitude of the initial power spectrum, defined as the root-mean-square mass density fluctuation within spheres of radius $8h^{-1}\text{Mpc}$ , extrapolated to $z = 0$ using linear theory $\sigma_8$ ; the amplitude of the initial power spectrum parametrized as $S_8 \equiv \sigma_8 \sqrt{\Omega_m/0.3}$ ; the neutrino matter density parameter $\Omega_\gamma$ . The table is from <a href="#">Schaye et al. (2023)</a> .....	<b>10</b>
<b>2.2</b>	Subgrid model parameters, the table is from <a href="#">Schaye et al. (2023)</a> ..	<b>13</b>
<b>3.1</b>	The best-fit double power-law parameters of the bolometric QLF at selected redshifts. The table is from <a href="#">Shen et al. (2020)</a> .....	<b>15</b>

# List of Figures

<b>1.1</b>	Cumulative number density of quasars in certain luminosity bands. The figure is from <a href="#">Shen et al. (2020)</a> .....	<b>4</b>
<b>1.2</b>	Comparison between dark matter-only (DMO) simulations and hydrodynamical simulations. The figure is from <a href="#">Vogelsberger et al. (2019)</a> .....	<b>6</b>
<b>1.3</b>	Schematic illustration of the extreme dynamic range of the length scales of the physical processes influencing the formation and evolution of galaxies. This figure is from <a href="#">Crain &amp; van de Voort (2023)</a>	<b>8</b>
<b>2.1</b>	Comparison of the box sizes and the resolutions of the FLAMINGO with other cosmological hydrodynamical simulations. The figure is from <a href="#">Schaye et al. (2023)</a> .....	<b>11</b>
<b>3.1</b>	The best-fit parameters of the global evolution model of the QLF for the observational data. The table is from <a href="#">Shen et al. (2020)</a> .....	<b>16</b>
<b>4.1</b>	The Quasar Luminosity Function from both the simulation and the observation at different redshifts. The red solid lines represent the QLFs at 6 different redshifts from the L1_m9 simulation. The blue shaded region is 68% confidence intervals from the observational data and the blue dashed lines show the median value of the observational data. ....	<b>19</b>
<b>4.2</b>	Cumulative Quasar Luminosity Function, the dashed colored lines are from FLAMINGO simulation and the shaded regions are from observations ( <a href="#">Shen et al. (2020)</a> ). The edges of the shaded region correspond to the results of global fit A and global fit B. ....	<b>20</b>
<b>4.3</b>	The projected correlation functions of quasars in FLAMINGO (2.8 cGpc). The colored dashed lines represent the simulation results with different luminosity cuts, the red solid line represents the observational data fitting results from <a href="#">Shen et al. (2009)</a> , and the red and brown dots represent the observational data from <a href="#">Eftekharzadeh et al. (2015)</a> and <a href="#">Shen et al. (2007)</a> .....	<b>22</b>

---

5.1	Eddington Ratio Distribution Function (ERDF) in bins of black hole mass. ....	24
5.2	Quasar luminosity functions in bins of Eddington ratio at $z = 0.2$ (upper left), $z = 1.0$ (upper right), $z = 2.0$ (middle left), $z = 3.0$ (middle right), $z = 4.0$ (lower left), and $z = 5.0$ (lower right). The red dashed-dotted lines represent the total QLFs. The solid colored lines are the decomposition of the QLFs. The shaded regions show the 68% confidence intervals from the fitting of the observational data. ....	25
5.3	Quasar luminosity functions in bins of the black hole mass at $z = 0.2$ (upper left), $z = 1.0$ (upper right), $z = 2.0$ (middle left), $z = 3.0$ (middle right), $z = 4.0$ (lower left), and $z = 5.0$ (lower right). The red dashed-dotted lines represent the total QLFs. The solid colored lines are the decomposition of the QLFs. The shaded regions show the 68% confidence intervals from the fitting of the observational data. ....	27
5.4	Left panel: best-fitting median ratio of stellar mass to peak halo mass ( $M_{\text{peak}}$ ) as a function of $M_{\text{peak}}$ and $z$ . Right panel: best-fitting median stellar mass as a function of $M_{\text{peak}}$ and $z$ . Errorbars in both panels show the 68% confidence interval for the model posterior distribution. The figure is from <a href="#">Behroozi et al. (2019)</a> .....	28
5.5	Quasar Luminosity Functions with different box sizes and resolutions. Different colors represent different simulations. The red solid lines represent the QLFs at 6 different redshifts from the L1_m9 simulation. The blue shaded region is 68% confidence intervals from the observational data and the blue dashed lines show the median value of the observational data. ....	29
5.6	Quasar Luminosity Functions with different cosmological variations. Different colors represent different cosmological variations. The red solid lines represent the QLFs at 6 different redshifts from the L1_m9 simulation. The blue shaded region is 68% confidence intervals from the observational data and the blue dashed lines show the median value of the observational data. ....	30
5.7	Quasar Luminosity Functions with different astrophysical variations. Different colors represent different astrophysical variations. The red solid lines represent the QLFs at 6 different redshifts from the L1_m9 simulation. The blue shaded region is 68% confidence intervals from the observational data and the blue dashed lines show the median value of the observational data. ....	32
5.8	Left panel: The correlation length as a function of redshift, different colors represent different luminosity threshold. Right panel: The correlation length as a function of luminosity, different colors represent different redshift. ....	33

<b>A.1</b>	Eddington ratio distribution function in bins of the luminosity. Different colors represent different luminosity ranges. ....	<b>37</b>
<b>A.2</b>	The DMH mass from clustering analysis as a function of redshift. The references are shown in the upper right of the figure. The red-shaded region represents the DMH mass range where most of quasars are expected to reside. This plot is from <a href="#">Arita et al. (2023)</a> .	<b>38</b>
<b>A.3</b>	Quasar luminosity functions in bins of the dark matter mass at $z = 0.2$ (upper left), $z = 1.0$ (upper right), $z = 2.0$ (middle left), $z = 3.0$ (middle right), $z = 4.0$ (lower left), and $z = 5.0$ (lower right). The red dashed-dotted lines represent the total QLFs. The solid colored lines are the decomposition of the QLFs. The shaded regions show the 68% confidence intervals from the fitting of the observational data. ....	<b>39</b>

# 1 . Introduction

In our work, we use the FLAMINGO simulation to study the Quasar Luminosity Function and the Quasar clustering. We will introduce some basic concepts and backgrounds related to our work in the following sessions.

## 1.1 Quasars and Supermassive Black Holes

### 1.1.1 Black holes and Supermassive Black Holes

According to general relativity, masses can curve the space. The more massive and compact the object, the larger distortion of the spacetime. General relativity predicts the existence of the event horizon, which is the boundary surrounding an object beyond which no light or other forms of radiation can escape. And we call this kind of object black hole. The first stellar mass black hole to be detected is Cygnus X-1 ([Webster & Murdin \(1972\)](#)).

It is believed that supermassive black holes (SMBHs), with masses ranging from millions to billions of solar masses are located at the center of the majority of galaxies. (e.g. [Kormendy & Richstone \(1995\)](#)). The existence of SMBHs was first suggested through the observation of high velocity gas and stellar motions near galactic centers, which indicated the presence of a massive, compact object. The masses of the SMBHs are correlated with the masses, luminosities and velocity dispersions of their host galaxy spheroids ([Kormendy & Richstone \(1995\)](#), [Ferrarese & Merritt \(2000\)](#), [Gebhardt et al. \(2000\)](#), [Gültekin et al. \(2009\)](#)).

The co-evolution of SMBHs and galaxies involves a cyclical process of star formation and feedback mechanisms. Stars form from very cold gas, which can also be accreted by the SMBH at the galaxy's center. As the SMBH consumes this gas, it emits powerful outflows—winds, jets, and radiation—that heat the surrounding cold gas, halting further star formation. This cessation stops the gas inflow into the SMBH. Over time, as the outflows diminish, the gas cools, allowing star formation to resume.

### 1.1.2 AGN

Active galaxies are a special class of galaxies characterized by intense activity or violent physical processes, such as energy production exceeding that of

stellar nuclear reactions, the generation of relativistic high-energy particles, non-thermal radiation, high-energy X-rays and gamma rays, and phenomena such as jets and explosions. However, these activities and processes predominantly occur in the cores of galaxies or originate from the cores. The core of an active galaxy is known as the active galactic nucleus (AGN).

Strictly defining an active galactic nucleus (AGN) is challenging, and there is no unified quantitative standard to date. Typically, AGNs are identified based on their main observational characteristics. The key observational features of AGNs include:

1. Luminous compact core region: The luminosity of AGNs ranges from  $10^{43}$  to  $10^{48}$  ergs $^{-1}$ , which is much higher than that of normal galaxies. However, the scale of AGNs is very small, generally believed to be less than 0.1 parsecs (pc).
2. AGNs exhibit strong atomic and ionic emission lines.
3. In certain wavelengths, such as radio, optical, and X-rays, AGNs exhibit non-thermal continuous radiation. Alternatively, the radiation in some wavelengths is thermal, or primarily thermal, but the thermal radiation does not originate from stars.
4. The intensity of continuous radiation, the strength and profile of emission lines, and polarization can vary over time.
5. AGNs have the capability to emit high-energy photons (X-rays and  $\gamma$  rays) much more strongly than normal galaxies.

### 1.1.3 Quasars and Supermassive black holes

Quasars are the extremely luminous AGNs. It is sometimes known as a quasi-stellar object. In 1960s, [Matthews & Sandage \(1963\)](#) identified an optical source around the radio source 3C 48. They found that the star-like object is much brighter than any other known galaxy with the absolute magnitude  $M = -24.3$  and the emitting volume of 3C 48 is much less than other identified sources. Moreover, there are several unknown broad emission lines in its spectrum. The discovery of quasars marked a significant milestone in the field of astronomy. In 1963, [Hazard et al. \(1963\)](#) utilized the opportunity presented by the lunar occultation of a radio source to accurately determine the position of the radio source 3C 273 using the Parkes 64 m radio telescope in Australia. They found that its optical counterpart was a star-like object with emission lines in its spectrum. Later that year, [Schmidt \(1963\)](#) used the Palomar Observatory's 5 m optical telescope to obtain the spectrum of this object. He identified that the emission lines were predominantly the hydrogen Balmer lines and determined the redshift of the emission lines to be  $z = 0.158$ . This discovery revealed that 3C 273 was not a star within our galaxy but a highly luminous object located at a significant distance, leading to the identification of quasars as a new class of astronomical objects.

The intrinsic luminosity of the quasars must be enormous, and so their mass. Quasars are thought to be fundamentally linked to supermassive black holes (SMBHs) at the centers of galaxies. The intrinsic link between quasars and SMBHs is fundamental to understanding their dynamics and impacts. The intense radiation emitted by quasars across the electromagnetic spectrum is primarily due to the accretion of gas and dust onto these SMBHs, which are pulled by the black hole's immense gravitational field. As these material accrete into the SMBHs, they heat up and release tremendous energy, illuminating the quasar. The high radiative efficiency makes quasars extremely luminous, allowing them to be detected even at great cosmic distances ([Mortlock et al. \(2011\)](#), [Venemans et al. \(2015\)](#), [Bañados et al. \(2017\)](#)). So AGNs and quasars serve as observable markers of these accreting supermassive black holes.

Two useful properties of quasars are the Quasar Luminosity Function (QLF), which is the comoving number density of quasars as a function of luminosity, and the Quasar clustering which describes the spatial distribution of quasars. These two properties can help us to understand how the luminosity of quasars evolves and what are the environments that can host quasar activities. The study of the Quasar Luminosity Function (QLF) and quasar clustering has a rich history, providing crucial insights into the evolution of quasars and their role in the universe.

### Quasar Luminosity Function

Early studies of the QLF in the rest-frame optical/UV (e.g. [Schmidt \(1968\)](#), [Boyle et al. \(1988\)](#), [Schmidt & Green \(1983\)](#)), the soft X-ray (e.g. [Boyle et al. \(1993\)](#)), hard X-ray (e.g. [Ueda et al. \(2003\)](#)), and IR (e.g. [Matute et al. \(2006\)](#)) have shown that the normalization and the slope of QLFs depends strongly on the redshift. These studies laid the foundation for understanding the distribution of quasar luminosities over cosmic time. [Hopkins et al. \(2006\)](#) provides a theoretical model that links the peak of quasar activity to galaxy mergers and peak star formation rates during cosmic noon. Studies by [Cowie et al. \(1996\)](#) and [Barger et al. \(2005\)](#) show that the number density of ANG with lower luminosity peaks at lower redshift. Figure 1.1 shows that the number density of quasars peaks at the cosmic noon and the location of the peak depends on the luminosity.

### Quasar clustering

Observational studies of quasar clustering (e.g. [La Franca et al. \(1998\)](#)) have provided evidence for increasing clustering amplitude with redshift, indicating that quasars are more clustered at earlier cosmic times. This observation aligns with findings from simulations ([Bonoli et al. \(2009\)](#); [Croton \(2009\)](#); [Degraf et al. \(2010\)](#)). Research by [Hopkins et al. \(2005\)](#) and [Hopkins et al. \(2006\)](#) examined the luminosity dependence of quasar clustering, suggesting that bright and faint quasars may populate the same dark matter halos, representing different phases of quasar evolution. In contrast, [Lidz et al. \(2006\)](#) proposed that different halo masses could indicate fundamentally different quasar populations.

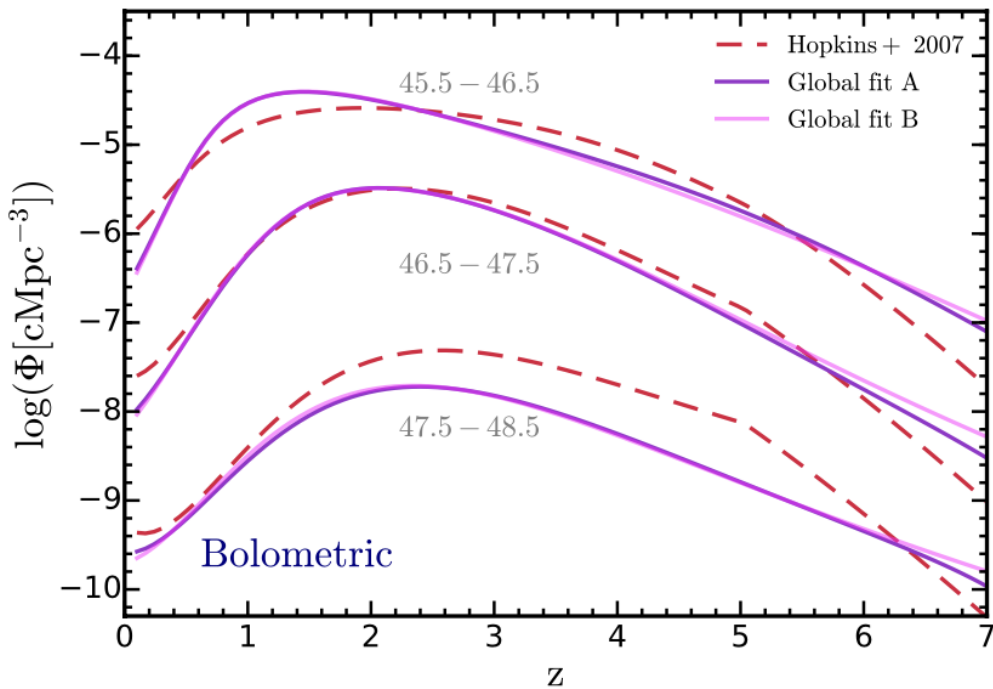


**Figure 1.1:** Cumulative number density of quasars in certain luminosity bands. The figure is from [Shen et al. \(2020\)](#)

## 1.2 Cosmological simulation

Cosmological simulations are powerful computational tools used to study the evolution of the universe from the Big Bang to the present day. These simulations model the dynamics of matter under the influence of gravity and other fundamental forces by inputting the basic laws of physics and initial conditions derived from observations.

The formation and evolution of galaxies are crucial aspects of large-scale cosmic evolution. Understanding galaxy formation and evolution is fundamental to our comprehension of the universe's structure and even fundamental physics. Galaxies possess many characteristics, including masses, star formation rates, morphology, and supermassive black holes at their centers. Due to the non-linearity of galaxy evolution, the involvement of various complex physical processes, and the limitations of current observations (such as resolution and distance), direct theoretical interpretation faces significant challenges. Therefore, cosmological simulations can help us better understand the evolution of the universe.

Various observations suggest that our universe is geometrically flat and that dark matter and dark energy dominate 95% of its energy density. The remaining 5% of the energy density is mainly comprised of baryons. The  $\Lambda$ CDM model posits that dark matter is cold and collisionless—so-called cold dark

matter—and that dark energy is represented by a cosmological constant ( $\Lambda$ ), which drives the accelerated expansion of the universe. The  $\Lambda$ CDM model can be used to understand galaxy formation and evolution.

Simulations require initial conditions to describe the initial fluctuations. The background of the universe can be described by a spatially flat Friedmann-Lemaître-Robertson-Walker metric. The power spectrum used to initialize simulations generally takes the form  $P(k) = Ak^n|T(k)|^2$ , which is a primordial power-law fluctuation field with a transfer function  $T(k)$ . The method to generate such Gaussian random fields with a specified power spectrum can be found in [Efstathiou et al. \(1985\)](#).

Dark matter structures provide the backbones for galaxy formation, with galaxies generally forming at the centers of halos. Therefore, simulations first need to model dark matter. In the  $\Lambda$ CDM model, dark matter is cold and collisionless, so in simulations, dark matter is modeled as a collisionless fluid, and its evolution is described by the collisionless Boltzmann function. Simulations that only model dark matter are known as dark matter only (DMO) simulations. In contrast to DMO simulations, hydrodynamical simulations model not only dark matter but also baryons. Therefore, simulating baryons is essential for making predictions about the observable Universe. The baryon component is mainly comprised of gas, mostly hydrogen and helium at the very beginning. Cosmic gas is assumed to be ideal, collisional and can be described by the Euler equations. Figure. 1.2 illustrates the difference between DMO simulations and hydrodynamical simulations. Dark matter-only simulations are used to predict the large-scale clustering of dark matter and its distribution within gravitationally bound dark matter halos. However, hydrodynamical simulations incorporate not only the gravitational effects of dark matter but also the complex interplay of baryonic matter, including gases, stars, and galaxies. They can provide much more detailed information about the 3D distribution, kinematics, temperature, and chemical composition of the gas.

### 1.3 Subgrid Model

Because different physical processes occur at different spatial scales, uniformly sampling representative cosmic volumes at the same resolution would require enormous computational power and memory. From Figure 1.3, we can see the spatial scales at which various physical processes occur. The evolution of the universe spans a vast range of scales, from the large-scale structure of the observable universe down to stars, covering approximately 36 orders of magnitude. Therefore, subgrid models remain a critical component of simulations of the galaxy population for the foreseeable future. Following are some physical processes treated with the subgrid models which are related to our work.

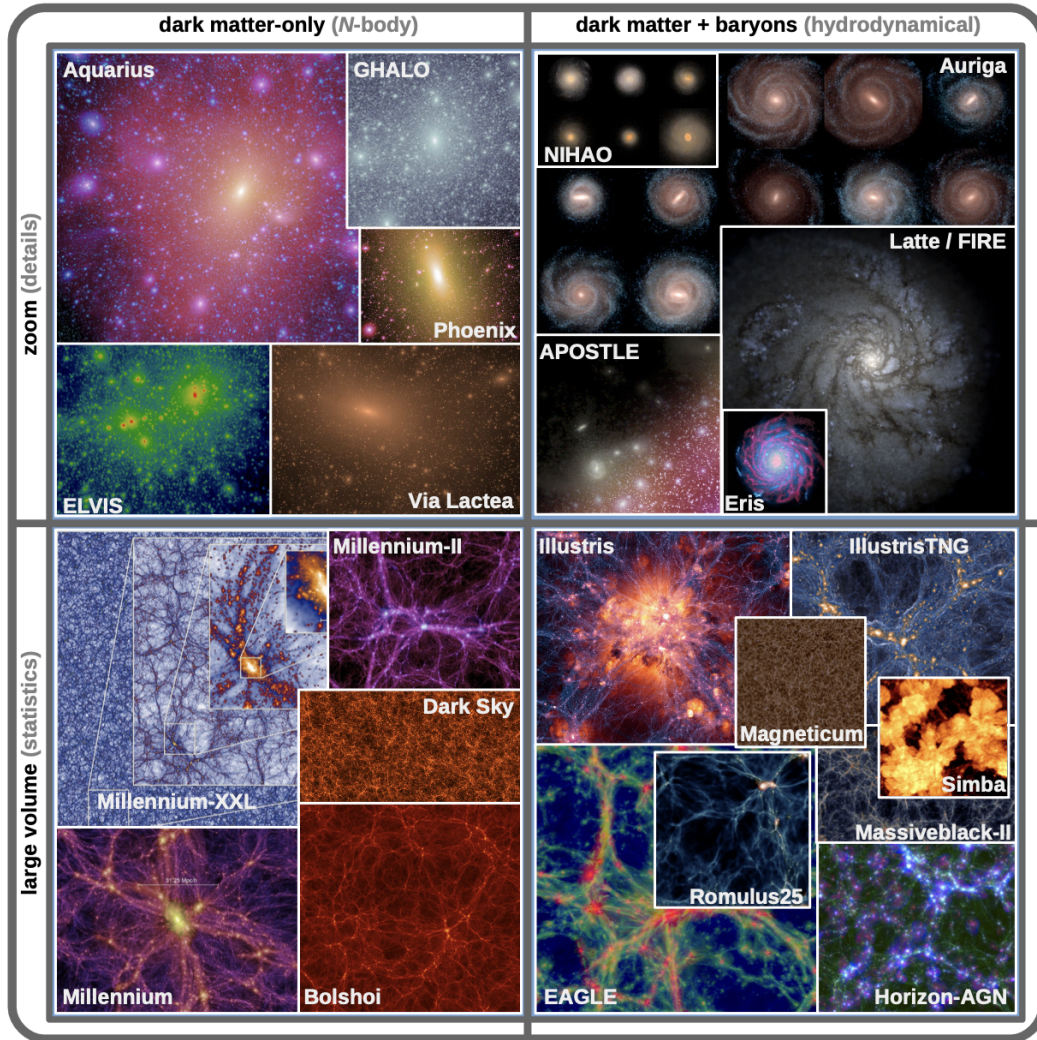


**Figure 1.2:** Comparison between dark matter-only (DMO) simulations and hydrodynamical simulations. The figure is from [Vogelsberger et al. \(2019\)](#)

### 1.3.1 SMBH seeding and growth

Supermassive black holes (SMBHs) are represented as collisionless sink particles. The seeds for SMBHs are placed either at the center of sufficiently massive halos that do not yet contain a black hole or within high-density gas that meets specific criteria ([Dubois et al. \(2012\)](#)). It is generally considered that the formation mass of SMBHs is smaller than the mass resolution of the simulation. Therefore, the seed particle of an SMBH has a subgrid mass in addition to its dynamical mass. The subgrid mass is used when calculating black hole accretion and mergers, while the dynamical mass is used for gravitational calculations. When the subgrid mass grows to match the dynamical mass, the two masses become equivalent.

The growth of black hole mass primarily occurs through two processes: accretion and mergers with other black holes. The accretion rate is typically

determined using the Eddington rate, which is the maximum rate at which a black hole can accrete matter while maintaining a balance between the outward radiation pressure and the inward gravitational pull, or the Bondi-Hoyle-Lyttleton rates (e.g. [Bondi & Hoyle \(1944\)](#)), or a modified version of the latter. The specific mathematical expressions will be detailed in Chapter 2. Black holes also grow through mergers, which are modeled in cosmological simulations as well. However, due to limitations in resolution, general relativistic effects are typically omitted, and it is presumed that the black holes merge immediately when they approach sufficiently close to each other.

### 1.3.2 AGN Feedback processes

Active Galactic Nucleus (AGN) feedback is a crucial mechanism in cosmological simulations that regulates the black hole growth and star formation. AGN feedback refers to the process by which energy and momentum from the central supermassive black hole (SMBH) are transferred to the surrounding gas in a galaxy. This can occur through various channels, such as radiation, winds, and jets, which can heat the gas, drive powerful outflows, and suppress star formation. By including AGN feedback in simulations, researchers aim to better understand its role in shaping the properties of galaxies, preventing runaway cooling and star formation, and maintaining the observed correlations between SMBHs and their host galaxies.

In simulations, AGN feedback is primarily divided into two modes: quasar mode and radio mode. The quasar mode refers to the phase in which a black hole rapidly grows under a high accretion rate, absorbing a large amount of matter and emitting intense radiation. This mode is commonly found in the early stages of galaxy formation in active galactic nuclei. On the other hand, the radio mode describes the phase where the black hole releases energy in the form of jets under a low accretion rate. This mode is typically associated with relatively low radiation and strong radio jets, significantly affecting the gas dynamics within galaxy clusters. In some simulations, due to resolution limitations, these two modes are not distinguished.

The quasar mode is associated with black hole accretion, and in simulations, it is typically assumed that a fraction,  $\epsilon_f$ , of the energy from AGN feedback is coupled to the surrounding interstellar medium (ISM). Therefore, the AGN feedback energy can be written as  $E_{\text{ANG}} = \epsilon_f \epsilon_r \dot{M}_{\text{BH}} c^2$ , where  $\dot{M}_{\text{BH}}$  is the black hole accretion rate and  $c$  is the speed of light ([Springel et al. \(2005\)](#)).

In radio mode feedback, the central supermassive black hole accretes material at a low rate, typically much below the Eddington limit. This lower accretion rate results in less luminous, but highly energetic, jet emissions, which are often associated with X-ray bubbles with enough energy to offset cooling losses. Therefore, this feedback mode is assumed to be important for the regulation of star formation in massive galaxies. In cosmological simulations, radio mode feedback is typically implemented using sub-grid models due to the infeasibility of directly resolving the detailed dynamics of relativistic jets. When the black hole accretion rate falls below a certain critical threshold, the radio mode feed-

back is activated. These models assume that the black hole releases energy in the form of jets, which can influence the intergalactic medium (IGM) and the gas dynamics within galaxy clusters on larger scales. The energy from these jets is usually injected into the surrounding environment as collimated relativistic particle streams or X-ray bubbles. This energy can heat the surrounding gas, counteracting cooling processes and suppressing star formation. In simulations, these feedback effects are realized by adjusting the temperature, density, and velocity of the surrounding gas. Although these sub-grid models can replicate the macroscopic effects of radio mode feedback to some extent, there remains significant uncertainty due to the large scale gap between the actual accretion and feedback processes and the scales that can be resolved in simulations.

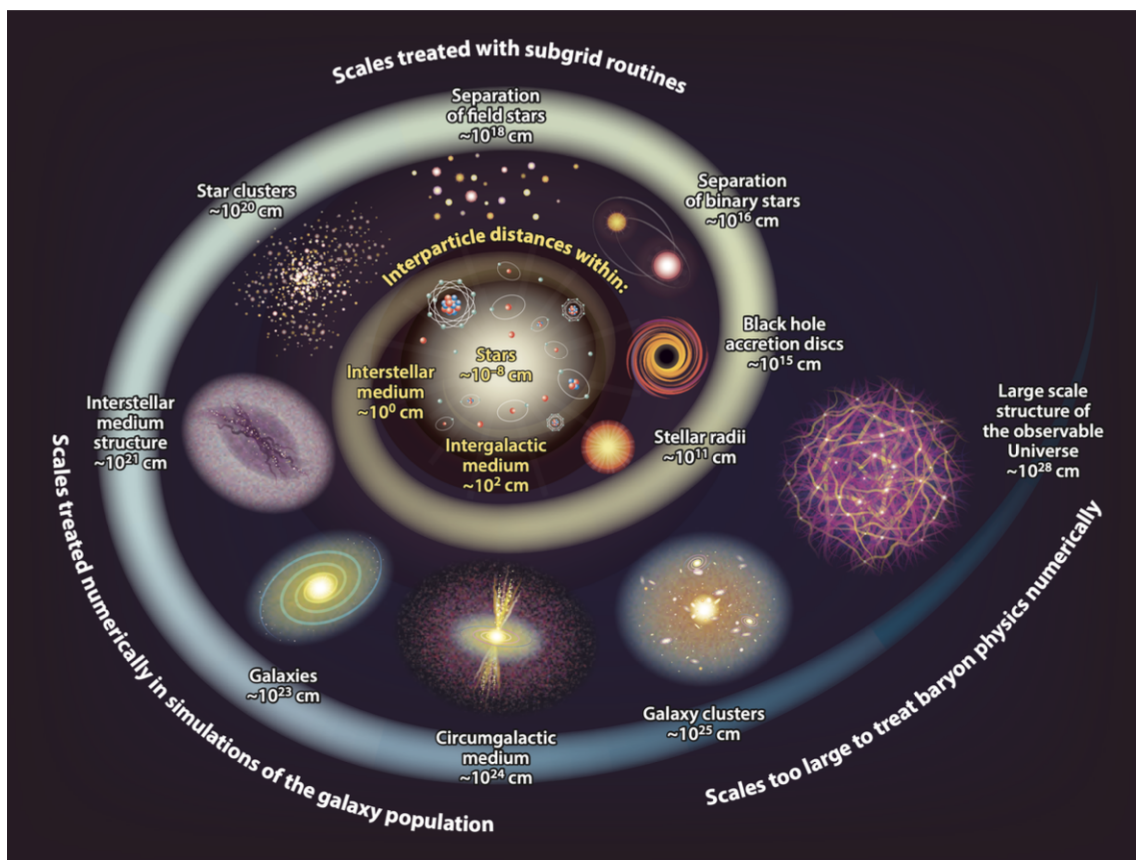


**Figure 1.3:** Schematic illustration of the extreme dynamic range of the length scales of the physical processes influencing the formation and evolution of galaxies. This figure is from [Crain & van de Voort \(2023\)](#)

In Chapter 2, we will give a general introduction to the simulation we used in our work. In Chapter 3, we focus on the calculation of the Quasar Luminosity Function and the quasar clustering. In Chapter 4, we display the results of our work. In Chapter 5, we analyse the difference between the simulation and the observation and probe the effect of different simulation variations on the results. And in Chapter 6, we give the conclusion of the whole work.

# 2 . Simulation

In this study, we use the simulation FLAMINGO published in [Schaye et al. \(2023\)](#). Here we present a brief summary of the simulation code and the method used.

## 2.1 FLAMINGO

The FLAMINGO simulation (Full-hydro Large-scale structure simulations with All-sky Mapping for the Interpretation of Next Generation Observations) is a cosmological hydrodynamical simulation for cosmology and galaxy cluster physics. The detailed introduction of the FLAMINGO can be found in [Schaye et al. \(2023\)](#). FLAMINGO uses three different resolutions: high resolution ( $1.3 \times 10^8 M_{\odot}$ ), intermediate resolution ( $1.1 \times 10^9 M_{\odot}$ ), and low resolution ( $8.6 \times 10^9 M_{\odot}$ ). The two main runs use volumes of  $(2.8 \text{ cGpc})^3$  and  $(1.0 \text{ cGpc})^3$  and baryonic particle masses of  $1 \times 10^9 M_{\odot}$  and  $1 \times 10^8 M_{\odot}$  respectively. The  $(2.8 \text{ cGpc})^3$  simulation is the largest ever hydrodynamical simulation run to  $z = 0$ . Figure 2.1 shows the comparison of the FLAMINGO with other hydrodynamical simulation. The cosmological parameters for the fiducial simulation in FLAMINGO is from the Dark Energy Survey year three (DES Y3; [Abbott et al. \(2022\)](#)). Besides the fiducial model, FLAMINGO includes eight astrophysics variations and four cosmology variations, all in  $(1.0 \text{ cGpc})^3$  volumes with intermediate resolution. The cosmological parameters for different cosmological variations can be found in Table 2.1. Moreover, FLAMINGO produces on-the-fly full-sky lightcone output for up to eight different observers.

The simulations were performed using the open source code `Swift` ([Schaller et al. \(2023\)](#)). The hydrodynamical equations are solved by `sphenix` flavour of smooth particle hydrodynamics (SPH) scheme ([Borrow et al. \(2022\)](#)). The massive neutrinos in FLAMINGO are modelled using ' $\delta f$ ' method which is designed to reduce shot noise ([Elbers et al. \(2021\)](#)). The initial condition is set up using a modified version of `Monofonic` code, which implements the effects of massive neutrinos ([Hahn et al. \(2021\)](#), [Elbers et al. \(2022\)](#)). The haloes and substructures were performed using `VELOCIRAPTOR` ([Elahi et al. \(2019\)](#)). The galaxy and cluster measurements were computed using the Spherical Over-density and Aperture Processor (SOAP). SOAP takes the (sub)halo centers and particle membership determined by `VELOCIRAPTOR` as input, and computes a

**Table 2.1:** Cosmological parameters in different simulations. The values from left to right are: The dimensionless Hubble constant  $h$ ; the total matter density parameter  $\Omega_m$ ; the dark energy density parameter  $\Omega_\Lambda$ ; the total baryonic matter density parameter  $\Omega_b$ ; the combined particle mass of all neutrino species  $\sum m_\nu$ ; the amplitude of the primordial matter power spectrum  $A_s$ , the primordial matter power spectral index  $n_s$ ; the amplitude of the initial power spectrum, defined as the root-mean-square mass density fluctuation within spheres of radius  $8h^{-1}\text{Mpc}$ , extrapolated to  $z = 0$  using linear theory  $\sigma_8$ ; the amplitude of the initial power spectrum parametrized as  $S_8 \equiv \sigma_8 \sqrt{\Omega_m/0.3}$ ; the neutrino matter density parameter  $\Omega_\gamma$ . The table is from [Schaye et al. \(2023\)](#)

Prefix	$h$	$\Omega_m$	$\Omega_\Lambda$	$\Omega_b$	$\sum m_\nu c^2$	$A_s$	$n_s$	$\sigma_8$	$S_8$	$\Omega_\gamma$
-	0.681	0.306	0.694	0.0486	0.06eV	$2.099 \times 10^{-9}$	0.967	0.807	0.815	$1.39 \times 10^{-3}$
Planck	0.673	0.316	0.684	0.0494	0.06eV	$2.101 \times 10^{-9}$	0.966	0.812	0.833	$1.42 \times 10^{-3}$
PlanckNuOp12Var	0.673	0.316	0.684	0.0496	0.12eV	$2.113 \times 10^{-9}$	0.967	0.800	0.821	$2.85 \times 10^{-3}$
PlanckNuOp24Var	0.662	0.328	0.672	0.0510	0.24eV	$2.109 \times 10^{-9}$	0.968	0.772	0.807	$5.87 \times 10^{-3}$
PlanckNuOp24Fix	0.673	0.316	0.684	0.0494	0.24eV	$2.101 \times 10^{-9}$	0.966	0.769	0.789	$5.69 \times 10^{-3}$
LS8	0.682	0.305	0.695	0.0473	0.06eV	$1.836 \times 10^{-9}$	0.965	0.760	0.766	$1.39 \times 10^{-3}$

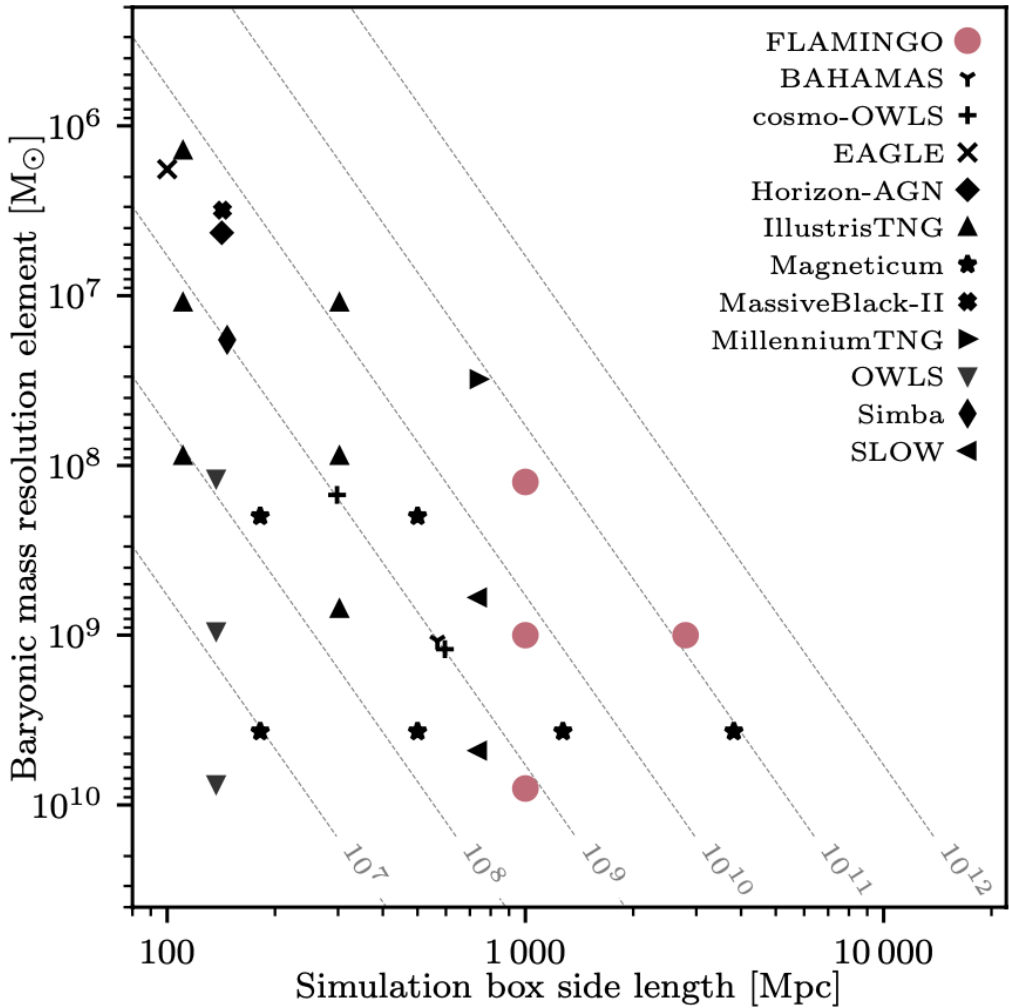


**Figure 2.1:** Comparison of the box sizes and the resolutions of the FLAMINGO with other cosmological hydrodynamical simulations. The figure is from [Schaye et al. \(2023\)](#)

large number of (sub)halo properties for a range of apertures, whose sizes can be specified as physical radii or mean internal overdensities.

The need to uniformly sample representative cosmic volumes restricts the feasible resolution of galaxy population simulations. Proposed mechanisms for supermassive black holes seeding are unresolved in FLAMINGO. Subgrid models were introduced in FLAMINGO to model these unresolved physical processes. The calibration of the subgrid physics is done by machine learning and the details can be found in [Kugel et al. \(2023\)](#). Following [Di Matteo et al. \(2008\)](#) and [Booth & Schaye \(2009\)](#), in FLAMINGO, seed black holes are placed in haloes that are sufficiently massive and do not yet contain a black hole. The haloes are found by running a friend-of-friend (FoF) halo finder with linking length 0.2 times the mean inter-particle distance at regular intervals. (The time interval is  $\Delta \log_{10} a = 1.00751$ ). The minimum halo mass for seeding is set to  $2.757 \times 10^{11} M_\odot$ . The seed of the black hole is positioned at the location of the densest gas

particle within the halo. This particle is then transformed into a collisionless black hole particle, assuming the mass of the original gas particle. Black hole processes are computed using the subgrid black hole mass, which is set to be  $10^5 M_\odot$ . And the gravitational force is computed using the seed particle mass.

The two modes of the black hole growth is through gas accretion and merging. In FLAMINGO, black holes merge if they are seperated by less than 3 gravitational softening lengths,  $r < 3\epsilon$ , and if their relative velocity satisfies  $\Delta v < \sqrt{2Gm_{\text{BH}}/r}$ , where  $m_{\text{BH}}$  is the mass of the most massive of the two black holes and  $r$  is the seperation.

Another growth mode is the gas accretion. According to [Springel et al. \(2005\)](#), black holes are accreted at a modified Bondi-Hoyle rate limited by the Eddington rate:

$$\dot{m}_{\text{accr}} = \alpha \frac{4\pi G^2 M_{\text{BH}}^2 \rho}{(c_s^2 + v^2)^{3/2}}, \quad (2.1)$$

where  $\rho$  and  $c_s$  are the gas density and the speed of sound of the ambient medium,  $v$  is the velocity of the black hole with respect to its enviroment, and the coefficient  $\alpha$  is a boost factor which is introduced because the simulations do not resolve the Bondi radius and the simulations do not model the multiphase ISM. Gas acrretion increases the black hole subgrid mass as

$$\dot{m}_{\text{BH}} = (1 - \epsilon_r) \dot{m}_{\text{accr}} \quad (2.2)$$

And decreases the black hole particle mass by  $\epsilon_r \dot{m}_{\text{accr}}$ . The decrease of the black hole particle mass accounts for the loss of rest mass to radiation, so the bolometric luminosity is

$$L = \epsilon_r \dot{m}_{\text{accr}} c^2 = \frac{\epsilon_r \dot{m}_{\text{BH}}}{1 - \epsilon_r} \quad (2.3)$$

Where the radiative efficiency is fixed to 0.1 in our work. The subgrid model parameters can be found in Table 2.2

In our work, we use L1<sub>m</sub>9 simulation to study the Quasar Luminosity Funtions. We also probe the effect of different variations on the results, including different boxsize and resolution, cosmological variations and astrophysical variation. We use L2p8<sub>m</sub>9 simulation to study the quasar clustering because it is the largest simulation run to  $z = 0$ .

**Table 2.2:** Subgrid model parameters, the table is from [Schaye et al. \(2023\)](#)

Prefix	$f_{SN}$	$\Delta v_{SN}$ ( $km\ s^{-1}$ )	$\Delta T_{AGN}$ or $v_{jet}$ ( $K$ ) or ( $km\ s^{-1}$ )	$\beta_{BH}$
Fid_m8	0.524	259	$10^{8.07}$	0.038
Fid_m9	0.238	562	$10^{7.95}$	0.514
Fid_m10	0	-	$10^{8.29}$	0.373
fgas + $2\sigma$ _m9	0.219	577	$10^{7.71}$	0.554
fgas - $2\sigma$ _m9	0.206	552	$10^{8.08}$	0.497
fgas - $4\sigma$ _m9	0.191	532	$10^{8.21}$	0.482
fgas - $8\sigma$ _m9	0.145	483	$10^{8.40}$	0.462
M* - $\sigma$ _m9	0.322	608	$10^{8.06}$	0.626
M* - $\sigma$ _fgas - $4\sigma$ _m9	0.261	557	$10^{8.27}$	0.620
Jet_m9	0.195	552	1585	0.501
Jet_fgas - $4\sigma$ _m9	0.176	527	1995	0.439

# 3. Methods

In this section, we introduce the methods we used to obtain Quasar Luminosity Functions (QLFs) and Quasar clustering.

## 3.1 Quasar Luminosity Function (QLF)

In alignment with our previous discussions, the radiation from black holes primarily originates from black hole accretion. Therefore, to calculate the luminosity of black holes, we begin with the accretion rate of the black holes. Utilizing equation 2.2, we are able to derive the luminosity of the black holes. We focus on a luminosity range from  $10^{42}$  to  $10^{48}$  ergs $^{-1}$ . This luminosity range is divided into several bins in logarithmic space. We define the interval of each bin as  $\Delta \log(L)$ , which represents the width of the luminosity interval in logarithmic units. We then count the number of quasars in each bin ( $N_i$ ) to compute the Quasar Luminosity Function (QLF), which is expressed as

$$\phi(L_i) = \frac{N_i}{(\text{boxsize})^3 \times \Delta \log(L)} \quad (3.1)$$

And the error is calculated using Poisson error

$$\Delta\phi(L_i) = \frac{\sqrt{N_i}}{(\text{boxsize})^3 \times \Delta \log(L)} \quad (3.2)$$

We also show the observational data compiled by [Shen et al. \(2020\)](#) in red lines, which includes observations in the rest-frame IR, B band, UV, soft and hard X-ray in the past decades. The quasar luminosity function is parameterized with a double power-law:

$$\phi_{\text{bol}} = \frac{dn}{d\log L} = \frac{\phi_*}{(L/L_*)^{\gamma_1} + (L/L_*)^{\gamma_2}} \quad (3.3)$$

We assume that all the four parameters follow a Gaussian distribution. The values listed in Table 3.1 represent the mean values, and the uncertainties correspond to the standard deviations of the Gaussian distribution. We randomly sample 1,000 sets of parameters and calculate the QLF for each set to obtain the median value and the error of the observational QLF.

**Table 3.1:** The best-fit double power-law parameters of the bolometric QLF at selected redshifts. The table is from [Shen et al. \(2020\)](#)

z	$\gamma_1$	$\gamma_2$	$\log\phi_*$	$\log L_*$
0.2	$0.787 \pm 0.024$	$1.713 \pm 0.046$	-4.240	$11.275 \pm 0.023$
1.0	$0.518 \pm 0.032$	$2.246 \pm 0.062$	$-4.320 \pm 0.064$	$12.347 \pm 0.0470$
2.0	$0.411 \pm 0.029$	$2.497 \pm 0.063$	$-4.678 \pm 0.046$	$13.011 \pm 0.032$
3.0	$0.424 \pm 0.070$	$1.878 \pm 0.058$	$-4.698 \pm 0.107$	$12.708 \pm 0.086$
4.0	$0.213 \pm 0.092$	$1.885 \pm 0.052$	-5.034	$12.5652 \pm 0.027$
5.0	$0.245 \pm 0.211$	$1.509 \pm 0.058$	-5.452	$11.978 \pm 0.055$

In order to get the evolution of the QLF, global fit on all the observational data at all the redshifts was done by [Shen et al. \(2020\)](#). There are two ways of fitting, we call them global fit A and global fit B. The difference between them is that the faint-end slope has a flexible polynomial evolutionary pattern for global fit A but is restricted to evolve monotonically with redshift has a power-law evolutionary pattern for global fit B. The four parameters we mentioned before evolve with redshift as:

$$\begin{aligned} \gamma_1(z) &= a_0 T_0(1+z) + a_1 T_1(1+z) + a_2 T_2(1+z) \\ \gamma_2(z) &= \frac{2b_0}{\left(\frac{1+z}{1+z_{\text{ref}}}\right)^{b_1} + \left(\frac{1+z}{1+z_{\text{ref}}}\right)^{b_2}} \\ \log L_*(z) &= \frac{2c_0}{\left(\frac{1+z}{1+z_{\text{ref}}}\right)^{c_1} + \left(\frac{1+z}{1+z_{\text{ref}}}\right)^{c_2}} \\ \log \phi_*(1+z) &= d_0 T_0(1+z) + d_1 T_1(1+z) \\ (T_0(x) &= 1, T_1(x) = x, T_2(x) = 2x^2 - 1) \end{aligned} \quad (3.4)$$

for glabal fit A, where  $T_n$  is the n-th order Chebyshev polynomial and  $z_{\text{ref}}$  is chosen to be 2. And for glabal fit B, there is a different evolution model at the faint end:

$$\gamma_1(z) = a_0 \left(\frac{1+z}{1+z_{\text{ref}}}\right)^{a_1} \quad (3.5)$$

where  $z_{\text{ref}}$  is also chosen to be 2. The best-fit parameters for the observational data can be found in Fig. 3.1. There are 11 parameters for global fit A and 10 parameters for global fit B. To get the error estimation for the cumulative quasar luminosity function, the same as what we did in the QLF part, we assume the Gaussian distribution for all the 11/10 parameters and randomly sample 1,000 sets of parameters to get the cumulative QLF and then the 68% confidence interval for these 1000 samples.

	Parameter	Best-fit A	Best-fit B
$\gamma_1$	$a_0$	$0.8569^{+0.0247}_{-0.0253}$	$0.3653^{+0.0115}_{-0.0114}$
	$a_1$	$-0.2614^{+0.0162}_{-0.0164}$	$-0.6006^{+0.0422}_{-0.0417}$
	$a_2$	$0.0200^{+0.0011}_{-0.0011}$	
$\gamma_2$	$b_0$	$2.5375^{+0.0177}_{-0.0187}$	$2.4709^{+0.0163}_{-0.0169}$
	$b_1$	$-1.0425^{+0.0164}_{-0.0182}$	$-0.9963^{+0.0167}_{-0.0161}$
	$b_2$	$1.1201^{+0.0199}_{-0.0207}$	$1.0716^{+0.0180}_{-0.0181}$
$L_*$	$c_0$	$13.0088^{+0.0090}_{-0.0091}$	$12.9656^{+0.0092}_{-0.0089}$
	$c_1$	$-0.5759^{+0.0018}_{-0.0020}$	$-0.5758^{+0.0020}_{-0.0019}$
	$c_2$	$0.4554^{+0.0028}_{-0.0027}$	$0.4698^{+0.0025}_{-0.0026}$
$\phi_*$	$d_0$	$-3.5426^{+0.0235}_{-0.0209}$	$-3.6276^{+0.0209}_{-0.0203}$
	$d_1$	$-0.3936^{+0.0070}_{-0.0073}$	$-0.3444^{+0.0063}_{-0.0061}$

**Figure 3.1:** The best-fit parameters of the global evolution model of the QLF for the observational data. The table is from [Shen et al. \(2020\)](#)

## 3.2 Quasar clustering

The Quasar clustering is described by the tow-points correlation function. The real-space correlation function is estimated using

$$\xi(r) = \frac{DD(r) - RR(r)}{RR(r)} \quad (3.6)$$

where  $RR(r)$  and  $DD(r)$  are the number of the random-random and data-data pairs enclosed in radius  $r$  respectively.  $DD(r)$  can be counted using CORRFUNC python package. For a series of radius  $r_i$ ,  $RR_i$  can be calculated as:

$$RR_i = \frac{4\pi}{3}(r_{i+1}^3 - r_i^3) \frac{N^2}{\text{boxsize}^3} \quad (3.7)$$

Where  $N$  is the number of the quasars. And the error can be calculated using Poisson error:

$$\Delta\xi(r) = \frac{\sqrt{DD(r)}}{RR(r)} \quad (3.8)$$

To determine the projected correlation function, we follow standard practice and compute the correlation function on a two-dimensional grid of pair separations parallel ( $\pi$ ) and perpendicular ( $r$ ) to the line of sight. Then the projected correlation function  $w_p(r_p)$  can be obtained by intergrating  $\xi_s(r_p, \pi)$  along the  $\pi$  direction:

$$w_p(r_p) = \int_{-\infty}^{\infty} \xi(r_p, \pi) d\pi \quad (3.9)$$

In practice, we integrate it to the cutoff value  $\pi_{\max} = 100 \text{ cMpc}$ . And the projected correlation function is related to the real-space correlation function via:

$$w_p(r_p) = 2 \int_{r_p}^{\pi_{\max}} \frac{r \xi(r)}{\sqrt{r^2 - r_p^2}} dr \quad (3.10)$$

### 3.3 Eddington Radio

The Eddington ratio is a dimensionless parameter used in astrophysics to measure the accretion rate of a black hole relative to its Eddington luminosity. The Eddington luminosity is the theoretical maximum luminosity a celestial body like a black hole can achieve when there is equilibrium between the radiation and the gravitational force. The Eddington luminosity can be calculated as:

$$L_{\text{edd}} = \frac{4\pi G M_{\text{BH}} m_p c}{\sigma_T} \quad (3.11)$$

So according to the definition of the Eddington ratio and the expression of the quasar luminosity from eq 2.3. Eddington ratio  $\lambda$  can be get from:

$$\lambda = \frac{L}{L_{\text{edd}}} = \frac{\epsilon_r \sigma_T}{4\pi G (1 - \epsilon_r) m_p c} \frac{\dot{M}_{\text{BH}}}{M_{\text{BH}}} \quad (3.12)$$

# 4 . Results

In this Chapter, we will show and give a brief explanation on the results of our work.

## 4.1 Quasar Luminosity Function

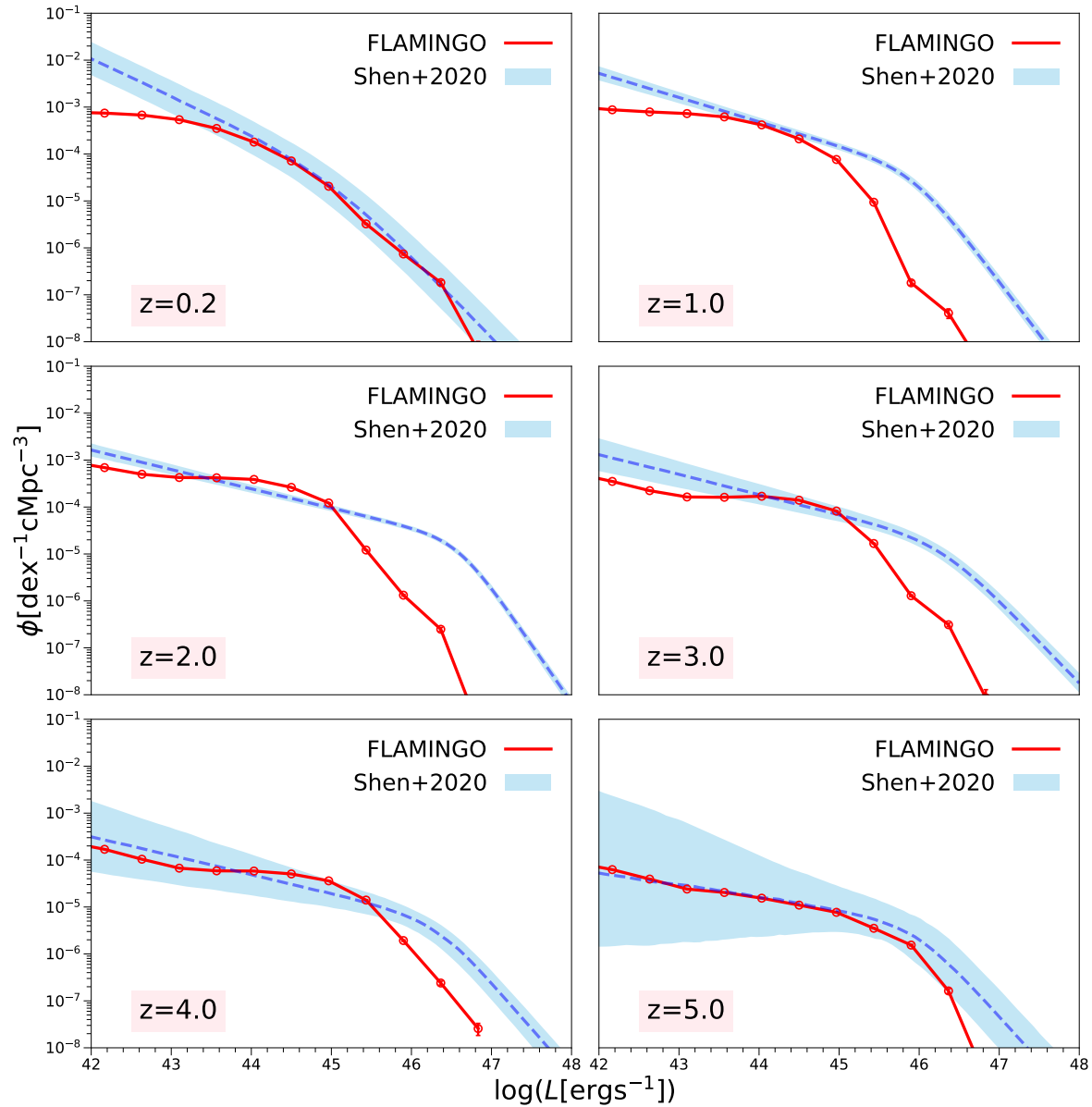
We employed the Spherical Overdensity (SO) catalog from the fiducial simulation with a box size of 1Gpc from the FLAMINGO simulation to calculate the quasar luminosity function (QLF) and the corresponding error bars. The specific computational process is discussed in Chapter 3.

Figure 4.1 illustrates the QLF across six different redshift ranges from  $z = 0.2$  to  $z = 5.0$ , alongside a comparison with observational data. The red lines represent the simulation results, while the blue shaded region indicates the 68% confidence interval of the observational data, with the blue dashed line marking the median of the observational data.

We find that at a redshift of  $z = 0.2$ , the simulation results are consistent with, or match well with, the observations. For redshifts  $z = 1.0, 2.0$ , and  $3.0$ , within the luminosity range of  $10^{43}$  to  $10^{45}$  ergs $^{-1}$ , the simulation results closely align with the observational data, although they underestimate the number of quasars at the bright end ( $L > 10^{45}$  ergs $^{-1}$ ). At redshifts  $z = 4.0$  and  $z = 5.0$ , compared to the cosmic noon periods at redshifts  $z = 1.0, 2.0$ , and  $3.0$ , the agreement between the simulation and observational data improves, but the underestimation at the bright end still persists. At the faint-end, the shaded region corresponds to the results of the extrapolation from observational data. Furthermore, in Chapter 5, we will address the impact of the simulation's resolution on the results. These factors contribute to the discrepancies observed between the simulation and the observational data at the faint-end.

## 4.2 Cumulative Quasar Luminosity Function

To understand the growth history of black holes, we also studied the cumulative quasar luminosity function (QLF). We used the same simulation as in the QLF section. For the simulation, after obtaining the quasar luminosity, we directly counted the number of quasars in each luminosity bin. For the observational



**Figure 4.1:** The Quasar Luminosity Function from both the simulation and the observation at different redshifts. The red solid lines represent the QLFs at 6 different redshifts from the L1\_m9 simulation. The blue shaded region is 68% confidence intervals from the observational data and the blue dashed lines show the median value of the observational data.

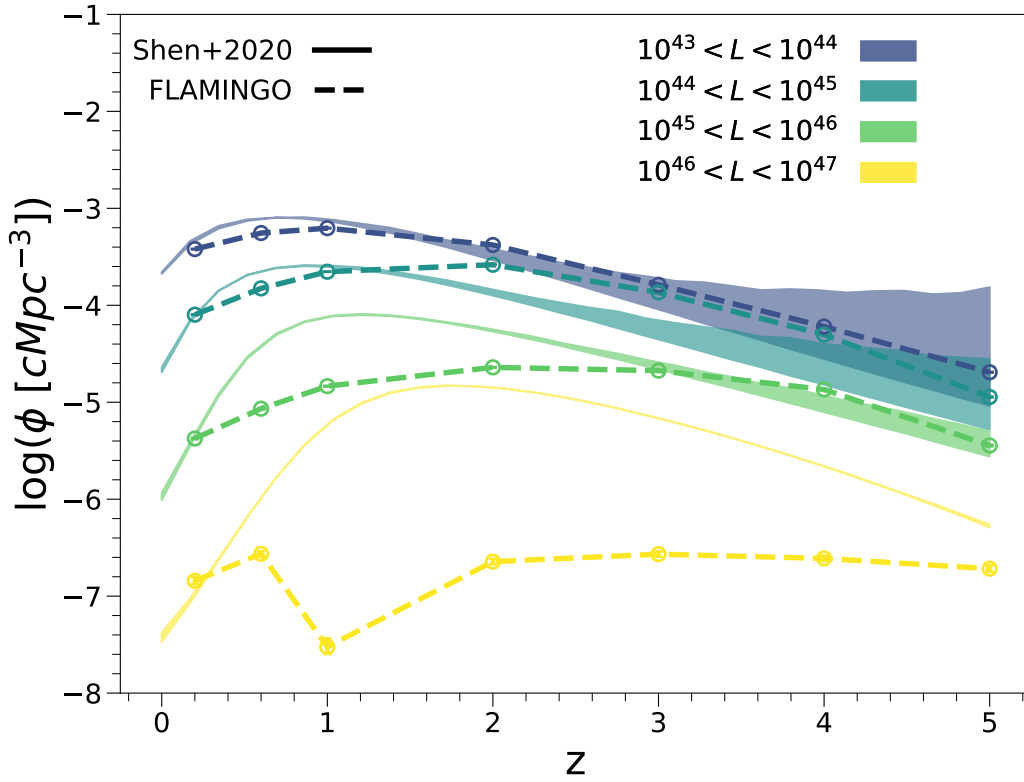


**Figure 4.2:** Cumulative Quasar Luminosity Function, the dashed colored lines are from FLAMINGO simulation and the shaded regions are from observations (Shen et al. (2020)). The edges of the shaded region correspond to the results of global fit A and global fit B.

data, we integrated and varied the integration limits according to Eq 3.3 to determine the number of quasars at fixed redshifts. In Figure 4.2, the dashed lines represent the cumulative QLFs of the simulation, while the shaded colored region represents the observational data. The edges of the shaded region correspond to the results of global fit A and global fit B. It can be found that different fits mainly affect the faint end of the cumulative QLF.

We found that the simulation overall matches the observations in the luminosity range of  $10^{43}$  to  $10^{44}$  ergs $^{-1}$ , with a consistent overall trend and a peak around cosmic noon. In the luminosity range of  $10^{44}$  to  $10^{45}$  ergs $^{-1}$ , the general trend is similar, but the simulation overestimates the number of quasars at redshift  $z = 2 - 4$ , which is also evident from the QLF plot. In the luminosity ranges of  $10^{45}$  to  $10^{46}$  ergs $^{-1}$  and  $10^{46}$  to  $10^{47}$  ergs $^{-1}$ , the simulation underestimates the number of quasars, particularly at redshifts corresponding to cosmic noon. Specifically, for the  $10^{46}$  to  $10^{47}$  ergs $^{-1}$  range, the simulation fails to reproduce the peak of the cumulative QLF at cosmic noon.

## 4.3 Quasar Clustering

In addition to studying the number of quasars, we are also concerned with their spatial distribution, so we investigated quasar clustering. We used the two-point correlation function to describe quasar clustering, with specific steps detailed in Chapter 3. We utilized the fiducial simulation from the FLAMINGO simulation with a box size of 2.8 Gpc, as this size provides more samples and reduces statistical errors. The range from 1 to 200 cMpc was evenly divided into logarithmic bins. Using the Corrfunc package, we counted the number of quasar pairs within each distance range and calculated the two-point correlation function using Eq 3.8. Then, we obtained the projected correlation function using Eq 3.10 with  $\pi_{max}$  set to be 100 cMpc.

Figure 4.3 shows the projected correlation function at different redshifts. The colored dashed lines represent the simulation results with different luminosity cuts, the red solid line represents the observational data fitting results from [Shen et al. \(2009\)](#), and the red and brown dots represent the observational data from [Eftekharzadeh et al. \(2015\)](#) and [Shen et al. \(2007\)](#). We found that in the low-redshift region ( $z < 4$ ), the simulation matches the observations very well, but at redshift  $z = 4$ , the simulation underestimates the correlation function. By studying the behavior of quasar clustering at different luminosity thresholds, we find that, in general, higher luminosity cuts correspond to higher correlation functions, indicating that quasars with higher luminosities are more clustered. Because we have the largest simulation to date, our work helps us study the clustering behavior of higher luminosity quasars.

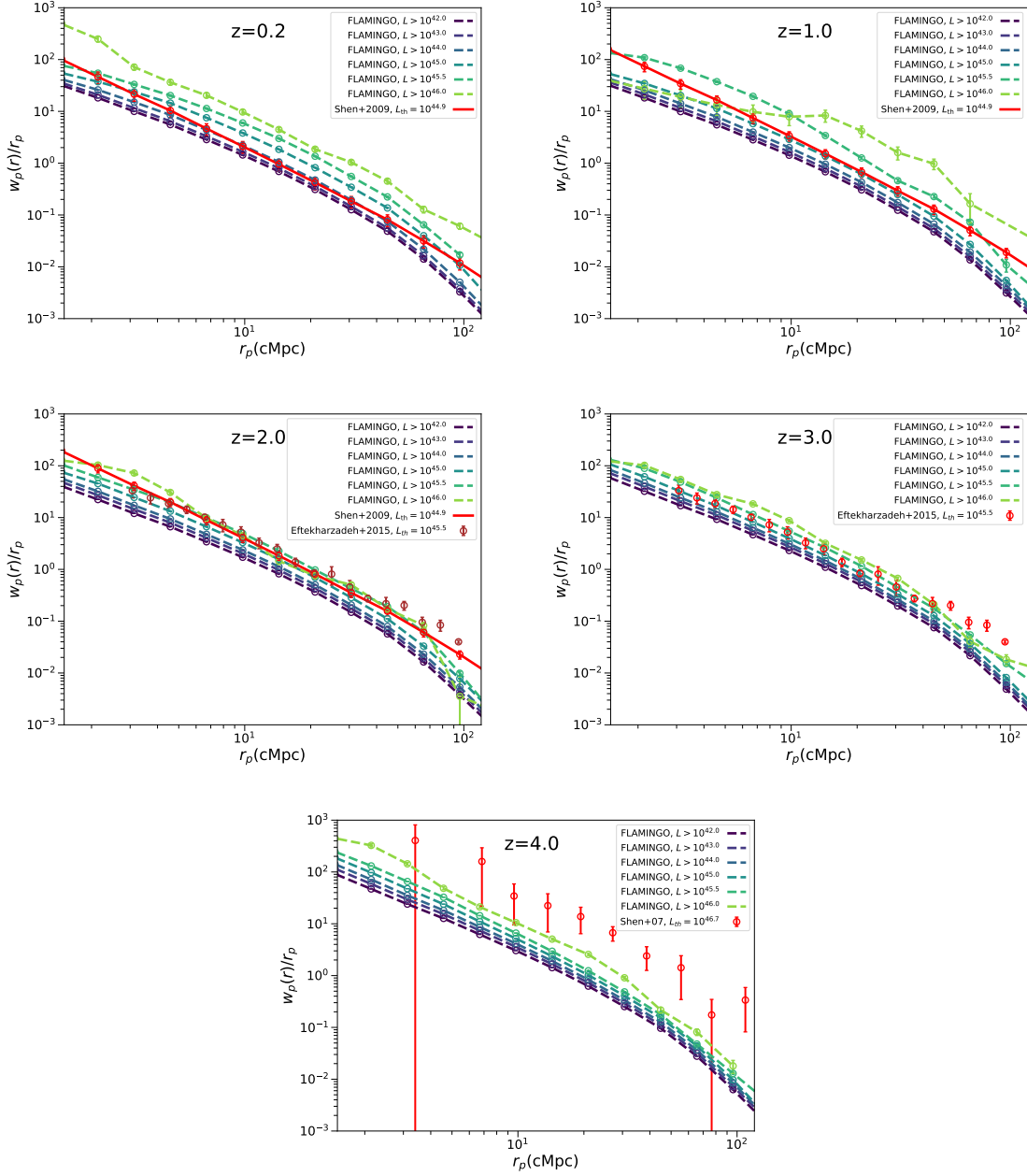


**Figure 4.3:** The projected correlation functions of quasars in FLAMINGO (2.8 cGpc). The colored dashed lines represent the simulation results with different luminosity cuts, the red solid line represents the observational data fitting results from [Shen et al. \(2009\)](#), and the red and brown dots represent the observational data from [Eftekhari et al. \(2015\)](#) and [Shen et al. \(2007\)](#)

# 5 . Discussion

In this chapter, we discuss the results of our work, focusing on the decomposition of the QLFs and different variations of the simulation.

## 5.1 Quasar Luminosity Function

To explain the differences in the QLFs at the bright end between the simulation and observations, we investigated the distribution of the Eddington ratio of quasars. The Eddington ratio is defined as the ratio of an object's (e.g., a star or black hole) luminosity to its Eddington luminosity. The Eddington ratio indicates the accretion rate of a black hole. We used the black hole mass  $M_{\text{BH}}$  and black hole accretion rate  $\dot{M}_{\text{BH}}$  from the fiducial simulation with a 1 Gpc box size in the FLAMINGO simulation to calculate the Eddington ratio for each quasar.

Figure 5.1 shows the Eddington Ratio Distribution Function (ERDF) in bins of black hole mass, where different colors represent different ranges of black hole mass. We find that the Eddington ratio mainly ranges between  $10^{-5}$  and 1.

To understand the dominated components of the QLFs at different luminosities, we decomposed the QLFs. Figure 5.2 shows the decomposition of QLFs by the Eddington ratio. The red dashed-dotted lines represent the total QLFs. The solid lines of different colors represent the QLFs for different ranges of Eddington ratios. The blue shaded region represents the 68% confidence interval of the observations, and the blue dashed lines show the median value of the observations. Figure 5.3 shows the decomposition of the QLFs by black hole mass, where the solid lines of different colors represent different ranges of black hole mass, and other representations are the same as before.

For the decomposition by Eddington ratio, we find that different segments of the QLFs are dominated by different Eddington ratios. The general trend is that higher luminosities correspond to higher Eddington ratios, which aligns with our intuitive understanding. For redshifts  $z = 0$  to 2, different Eddington ratios dominate different segments of the QLFs. At the bright end of the QLFs, the Eddington ratios range from 0.01 to 1. For redshifts  $z = 3$  to 5, within the range shown in our plot, the Eddington ratios are mostly between 0.1 and 1, indicating that these SMBHs are accreting close to the Eddington rate. Considering the distribution characteristics of the Eddington ratio in the ERDF, we can speculate

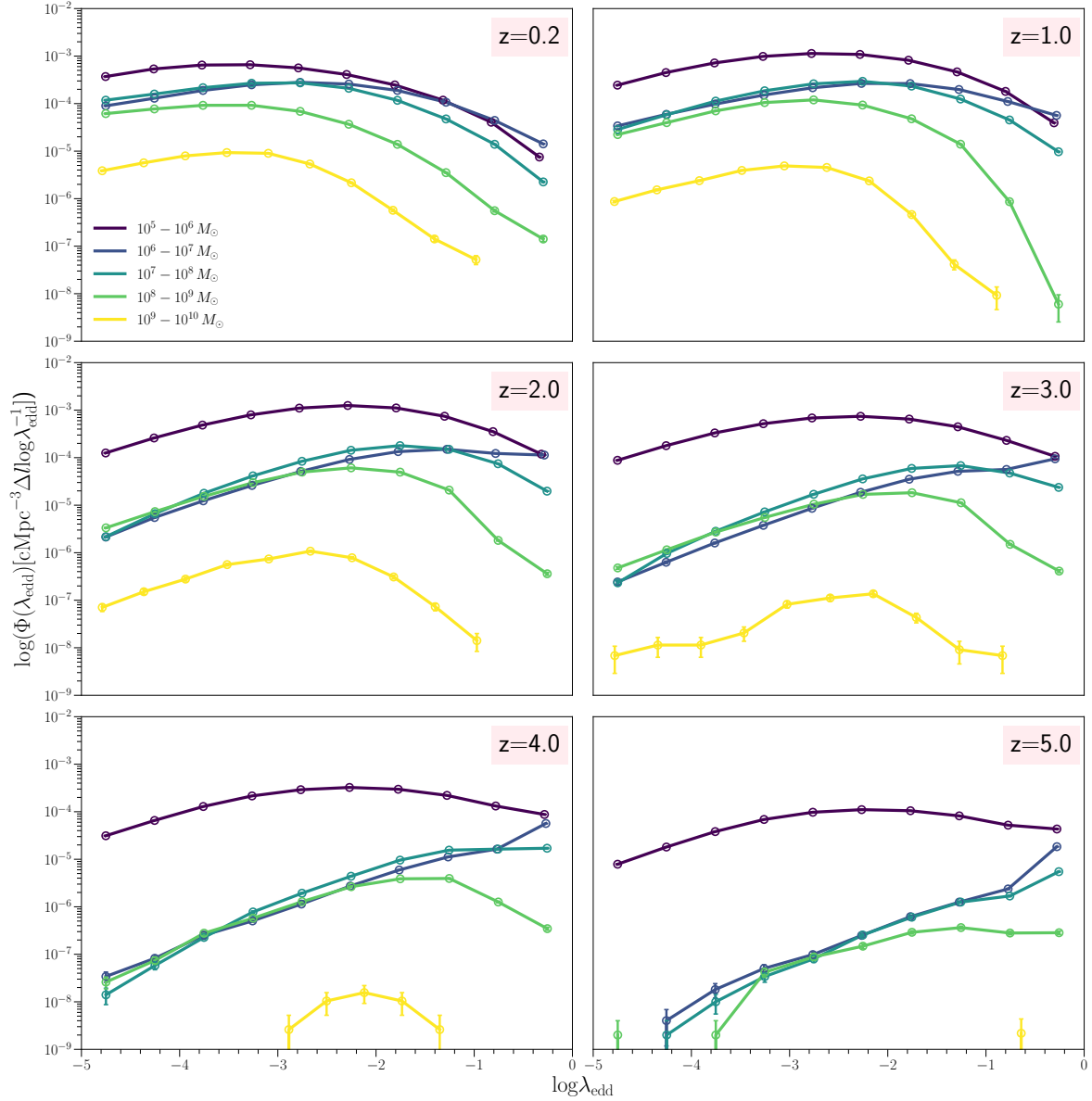


**Figure 5.1:** Eddington Ratio Distribution Function (ERDF) in bins of black hole mass.

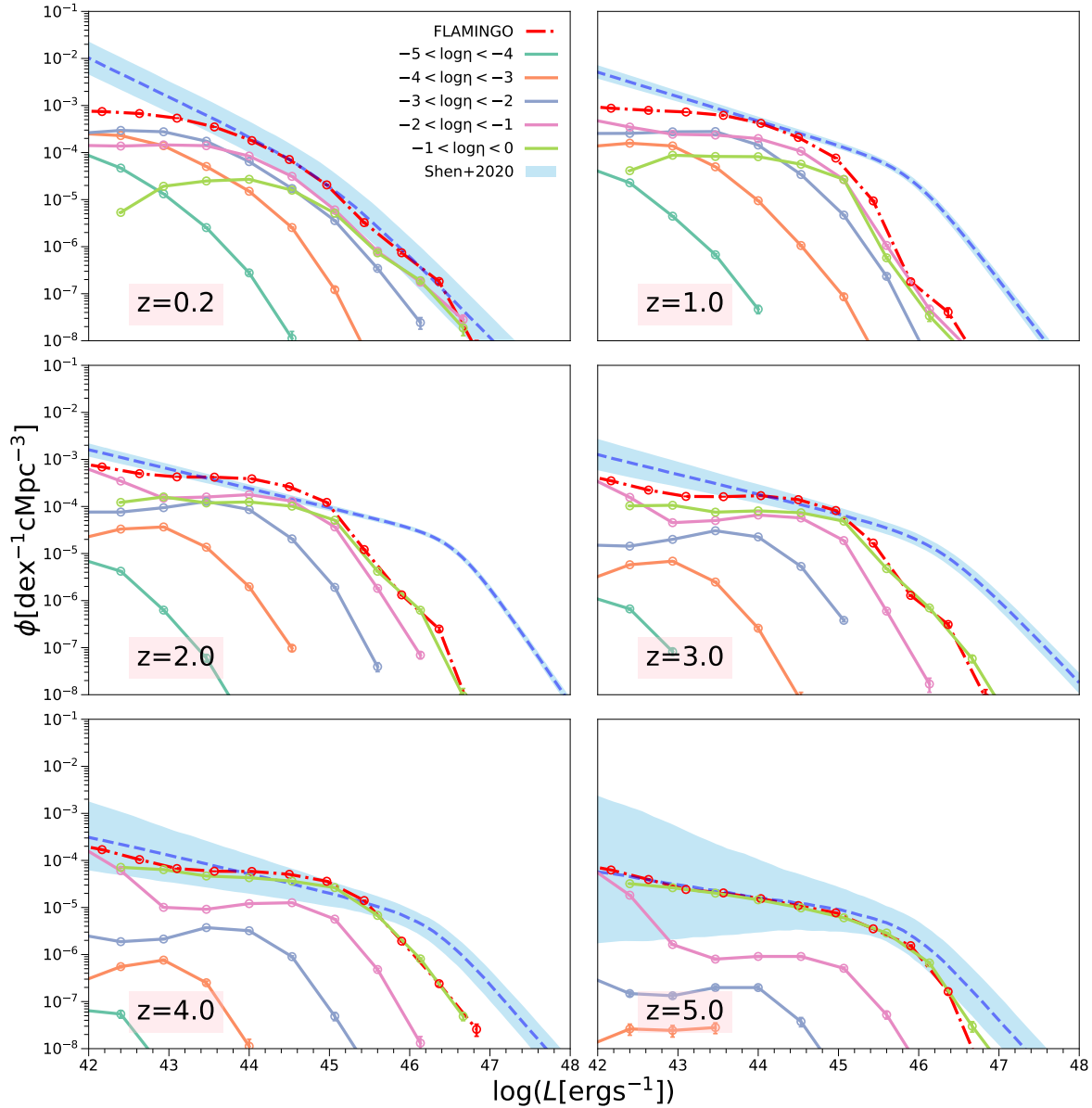


**Figure 5.2:** Quasar luminosity functions in bins of Eddington ratio at  $z = 0.2$  (upper left),  $z = 1.0$  (upper right),  $z = 2.0$  (middle left),  $z = 3.0$  (middle right),  $z = 4.0$  (lower left), and  $z = 5.0$  (lower right). The red dashed-dotted lines represent the total QLFs. The solid colored lines are the decomposition of the QLFs. The shaded regions show the 68% confidence intervals from the fitting of the observational data.

that one of the reasons for the differences between the bright end of the simulation and observations is the absence of super-Eddington ratios in FLAMINGO. As mentioned in Chapter 2, in the simulation chapter, we described the method used by FLAMINGO to simulate black holes, where the black hole accretion rate is set to a modified Bondi-Hoyle rate limited by the Eddington ratio. This supports our previous hypothesis.

For the decomposition by black hole mass in Figure 5.3, we find similar results to the Eddington ratio decomposition, where different black hole masses dominate different segments of the QLFs. The overall trend is that higher black hole masses correspond to higher luminosities. At redshifts  $z = 0$  to 1, the bright end of the QLF ( $L > 10^{45} \text{ ergs}^{-1}$ ) is mainly dominated by black hole masses  $10^8 < M_{\text{BH}} < 10^9 M_{\odot}$  and  $10^9 < M_{\text{BH}} < 10^{10} M_{\odot}$ . At redshifts  $z > 2$ , the bright end is mainly dominated by  $10^8 < M_{\text{BH}} < 10^9 M_{\odot}$ . We find that the green line decreases, indicating that these massive black holes became inactive.

This leads us to a second hypothesis: Another possible reason is that these active SMBHs, through powerful radiation and jets, heated and expelled the gas within galaxies, preventing further star formation through feedback processes. This feedback reduced the amount of cold gas available for accretion, leading to a decline in SMBH activity. As a result, these galaxies transitioned to a quenched state, where star formation was suppressed, and the SMBHs became inactive due to the lack of accretion material. According to [Behroozi et al. \(2019\)](#), in Figure 5.4, we can see the relationship between the stellar mass-peak halo mass ratio and stellar mass concerning peak halo mass, with different colors representing different redshifts. We can see a peak in the stellar mass-peak halo mass ratio at  $10^{12} < M_{\text{halo}} < 10^{13} M_{\odot}$ . From the right panel, we can see that for halos with redshifts less than 4, the stellar mass is relatively flat in the  $10^{12} < M_{\text{halo}} M_{\odot}$  range, indicating that the star formation process is weakened, which supports our previous viewpoint. Returning to our work, this is also reflected in the ERDF plot Figure 5.1. We can see that for the green line of black hole masses  $10^8 < M_{\text{BH}} < 10^9 M_{\odot}$ , there is a significant decrease in the high Eddington ratio segment with decreasing redshift, indicating that these SMBHs became inactive around cosmic noon, leading to an underestimation of the number of quasars at the bright end in the simulation.

## 5.2 Variations of the simulation

In this section, we present and discuss the effects of different variations on the QLFs.

### 5.2.1 Box sizes and Resolutions

Figure 5.5 shows the QLFs under different box sizes and resolutions. In the naming convention of the simulations, the first number represents the simulation box size, and the second number indicates the simulation resolution (e.g., L1000N1800 denotes a simulation with a box size of 1000 Mpc containing  $1800^3$

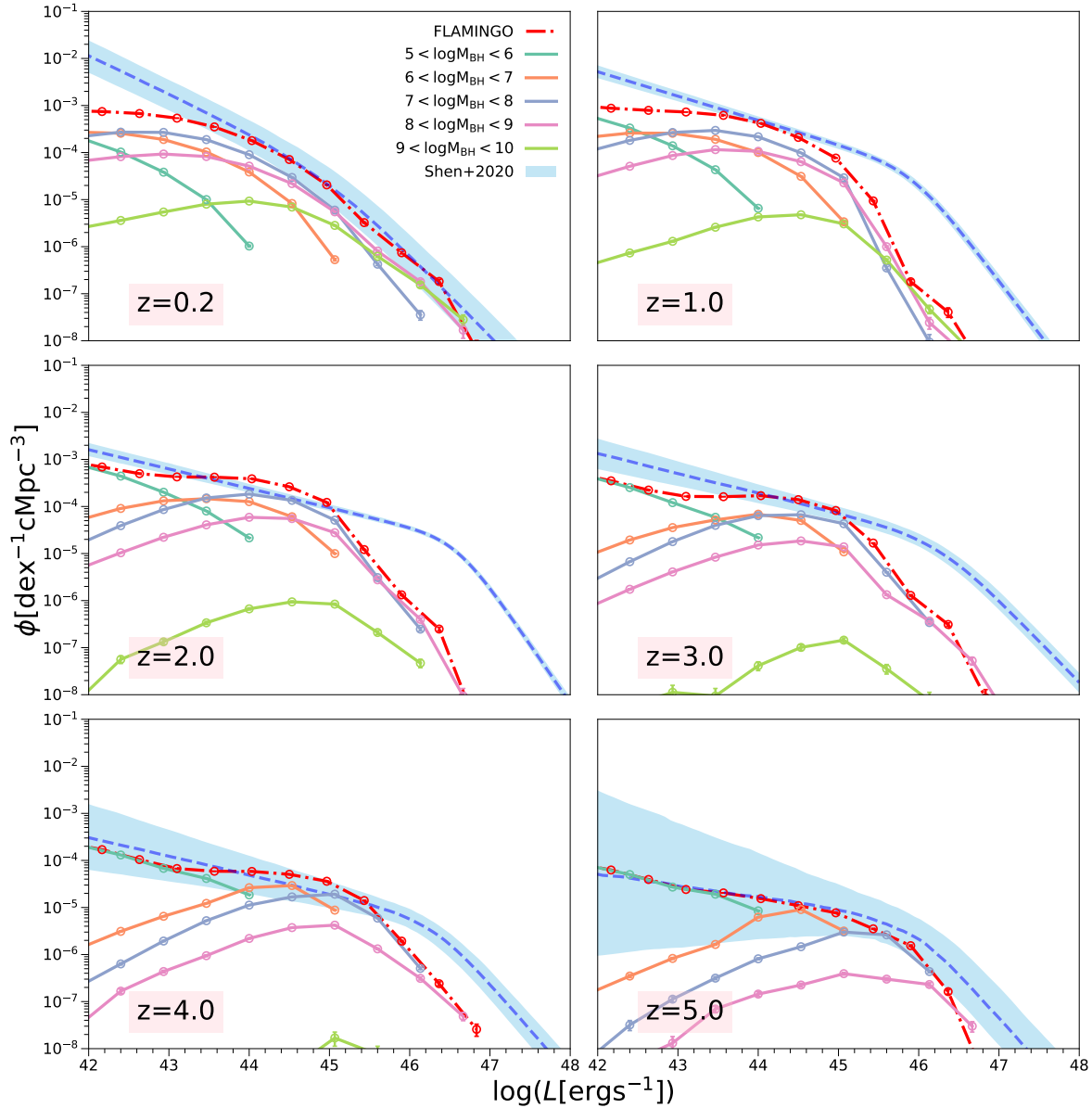


**Figure 5.3:** Quasar luminosity functions in bins of the black hole mass at  $z = 0.2$  (upper left),  $z = 1.0$  (upper right),  $z = 2.0$  (middle left),  $z = 3.0$  (middle right),  $z = 4.0$  (lower left), and  $z = 5.0$  (lower right). The red dashed-dotted lines represent the total QLFs. The solid colored lines are the decomposition of the QLFs. The shaded regions show the 68% confidence intervals from the fitting of the observational data.

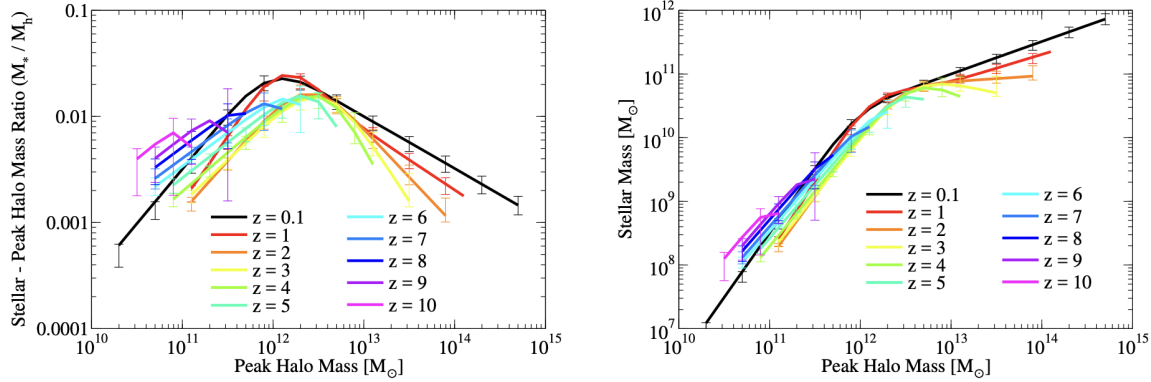


**Figure 5.4:** Left panel: best-fitting median ratio of stellar mass to peak halo mass ( $M_{\text{peak}}$ ) as a function of  $M_{\text{peak}}$  and  $z$ . Right panel: best-fitting median stellar mass as a function of  $M_{\text{peak}}$  and  $z$ . Errorbars in both panels show the 68% confidence interval for the model posterior distribution. The figure is from [Behroozi et al. \(2019\)](#)

particles). There are two box sizes: 1 Gpc and 2.8 Gpc. For the 1 Gpc box size, there are three resolutions: high resolution, intermediate resolution, and low resolution. The colored lines in the figure represent different simulations, the blue shaded region is the 68% confidence interval of the observational data, and the dashed blue line is the median value of the observations.

We find that the effect of different box sizes on the results is minimal, as evidenced by the nearly overlapping magenta and orange lines in the figure. The impact of resolution on the results is more significant, especially at the low luminosity end. For the previously mentioned differences between the simulation and observation at the faint end, the limitation of resolution is a potential factor. Additionally, resolution affects the cumulative QLFs, which may also contribute to the underestimation of the cumulative QLFs in the simulation. Our work demonstrates the impact of resolution on studying the number of quasars.

### 5.2.2 Cosmological Variations

We also compared the effects of different cosmological variations on the results, using simulations with different cosmology parameters under a 1 Gpc box size. The various cosmology parameters are listed in Chapter 2. In Figure 5.6, different colors represent different cosmological variations, while the rest of the figure follows the same conventions as before. We find that at low redshifts ( $z = 0 - 1$ ), the lines nearly overlap, indicating that cosmological variation has little effect on the QLFs in this range. At higher redshifts ( $z > 1.0$ ), we observed that the results for HYDRO\_FIDUCIAL and HYDRO\_PLANCK nearly overlap, while the results for HYDRO\_LOW\_SIGMA8 are slightly lower than the other two. Overall, HYDRO\_FIDUCIAL and HYDRO\_PLANCK align more closely with the observational data.

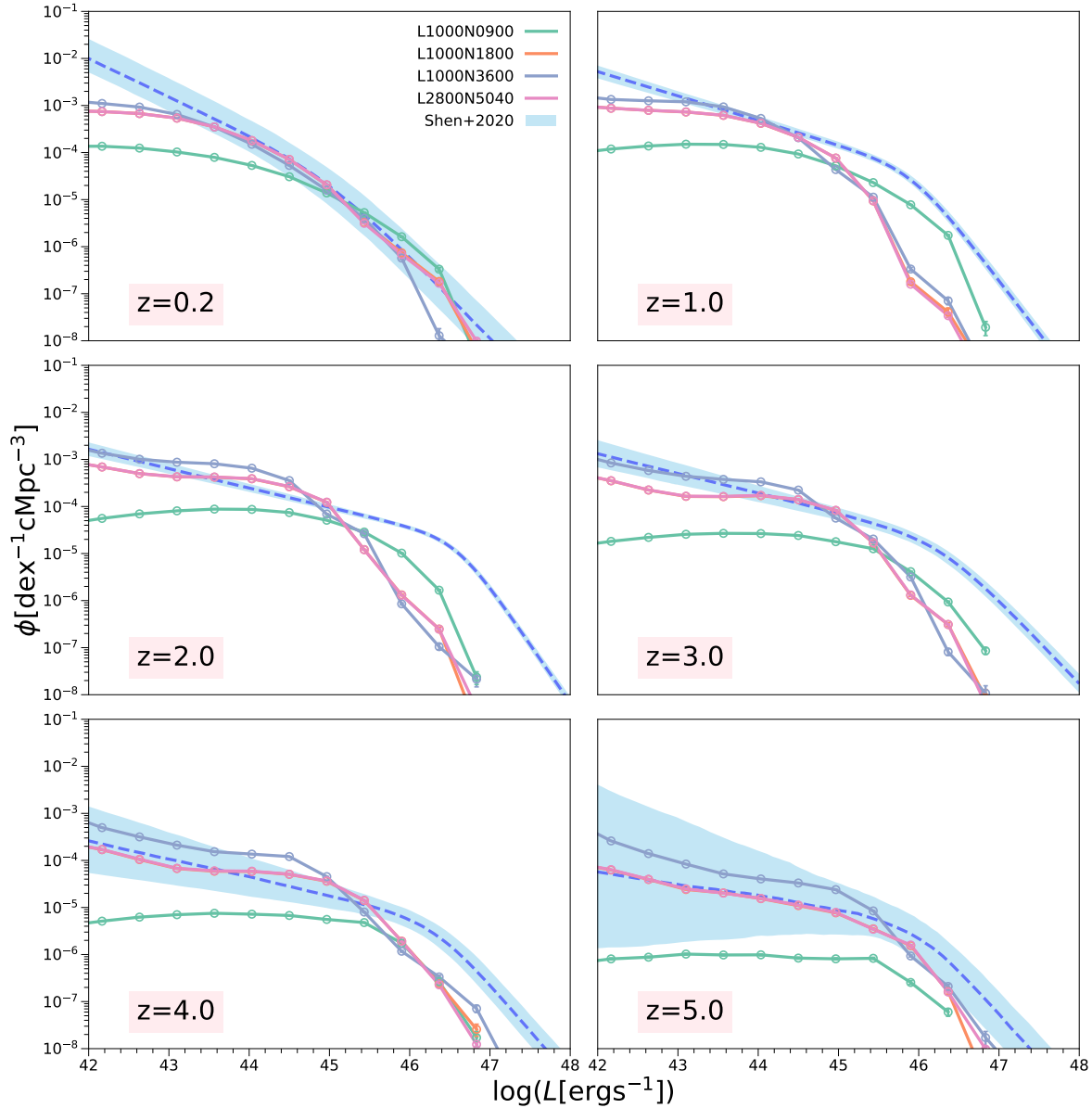


**Figure 5.5:** Quasar Luminosity Functions with different box sizes and resolutions. Different colors represent different simulations. The red solid lines represent the QLFs at 6 different redshifts from the L1\_m9 simulation. The blue shaded region is 68% confidence intervals from the observational data and the blue dashed lines show the median value of the observational data.

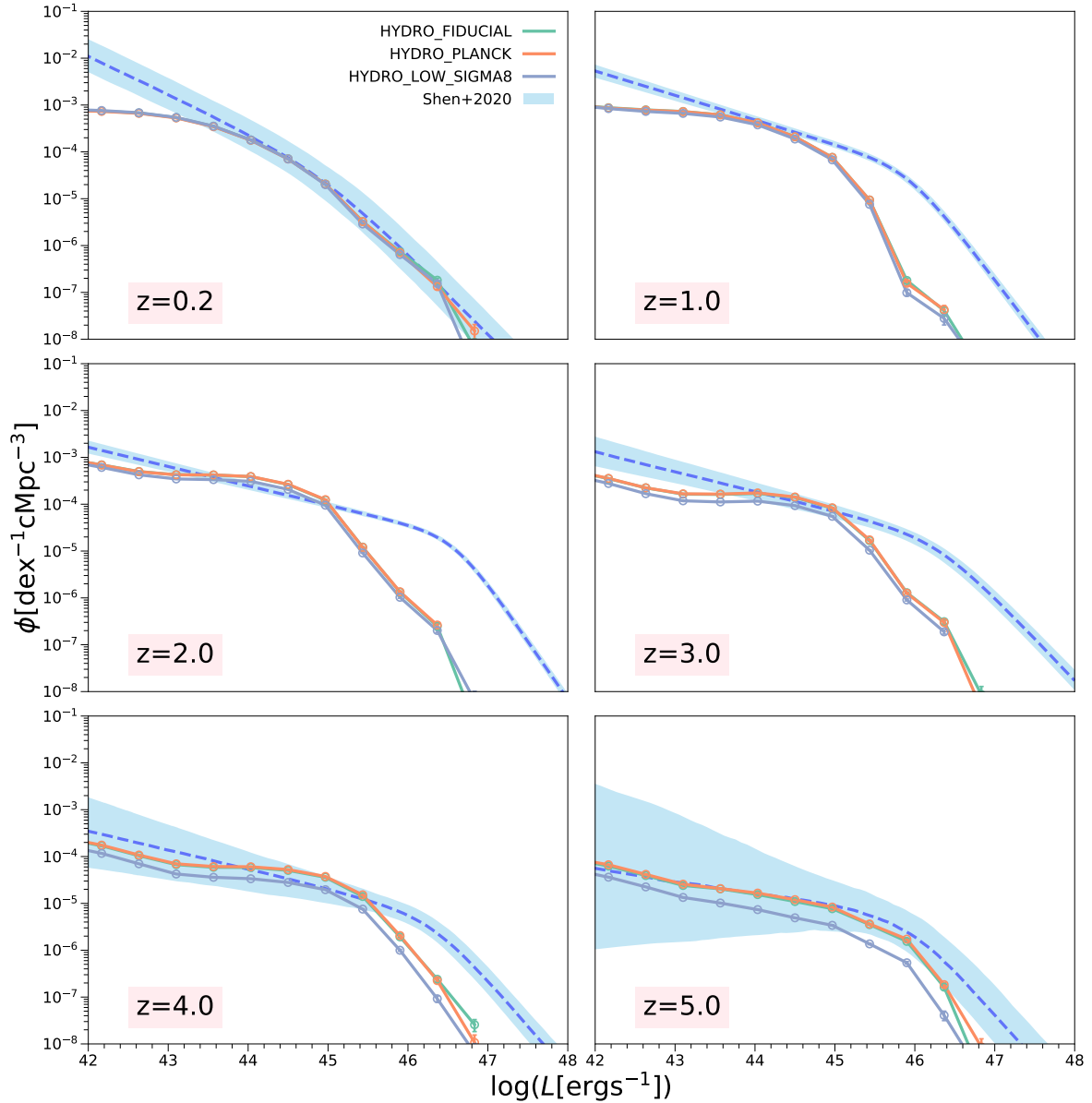


**Figure 5.6:** Quasar Luminosity Functions with different cosmological variations. Different colors represent different cosmological variations. The red solid lines represent the QLFs at 6 different redshifts from the L1\_m9 simulation. The blue shaded region is 68% confidence intervals from the observational data and the blue dashed lines show the median value of the observational data.

### 5.2.3 Astrophysical Variations

In addition to the fiducial simulation, FLAMINGO includes eight astrophysical variations, with specific parameters detailed in Chapter 2. All these simulations have a box size of 1 Gpc. In Figure 5.7, different colors represent different astrophysical variations, with other representations consistent with previous figures. We find that at the low luminosity end, the differences between the various astrophysical variations are not significant. At the bright end, there is better agreement between the simulation and the observational data for the QLFs with jet runs.

## 5.3 Correlation length

In this section, we focus on the clustering properties characterized by the correlation length, which is defined as the distance at which the correlation function is 1. We computed the two-point correlation function and derived the correlation length using interpolation methods.

The left panel of Figure 5.8 shows the correlation length as a function of redshift for the fiducial simulation with a box size of 2.8 Gpc, with different cuts in luminosity. The right panel displays the correlation length as a function of the lower-luminosity cut from  $z = 0$  to 4. From the left panel, we observe that the overall trend is a slight increase in correlation length with increasing redshift. At a fixed redshift, the correlation length increases with the luminosity threshold. Regarding the weird behavior of the correlation length at high luminosity thresholds and low redshifts, we examined the two-point correlation function and found that due to the limited number of simulated quasars, the two-point correlation function becomes noisy at low redshift and high luminosity, thereby affecting the calculation of the correlation length. The right panel yields similar results, and we also find a slight increase in the slope of the lines with increasing luminosity. This underscores the importance of larger simulations in studying the clustering behavior of higher luminosity quasars.

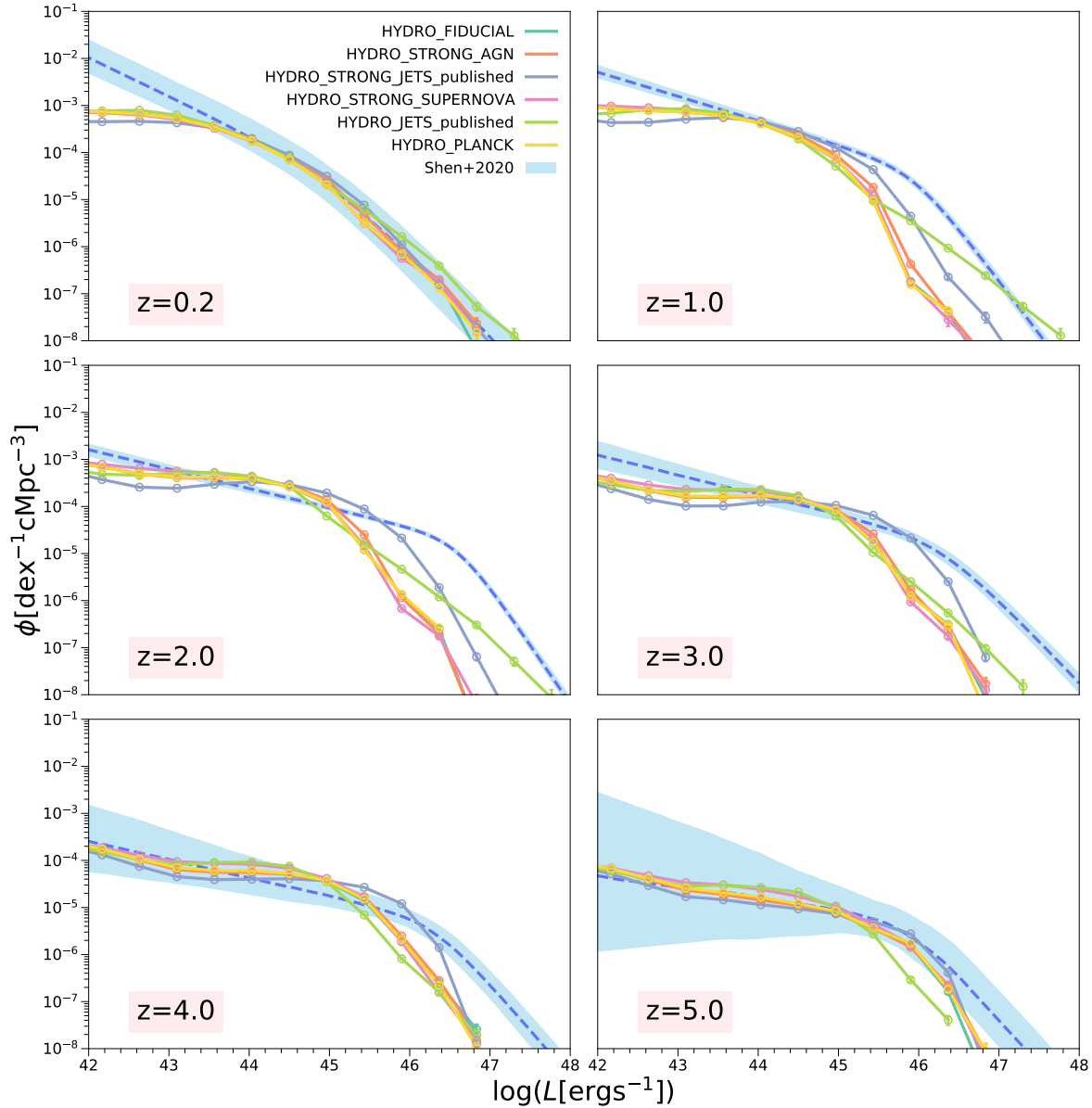


**Figure 5.7:** Quasar Luminosity Functions with different astrophysical variations. Different colors represent different astrophysical variations. The red solid lines represent the QLFs at 6 different redshifts from the L1\_m9 simulation. The blue shaded region is 68% confidence intervals from the observational data and the blue dashed lines show the median value of the observational data.

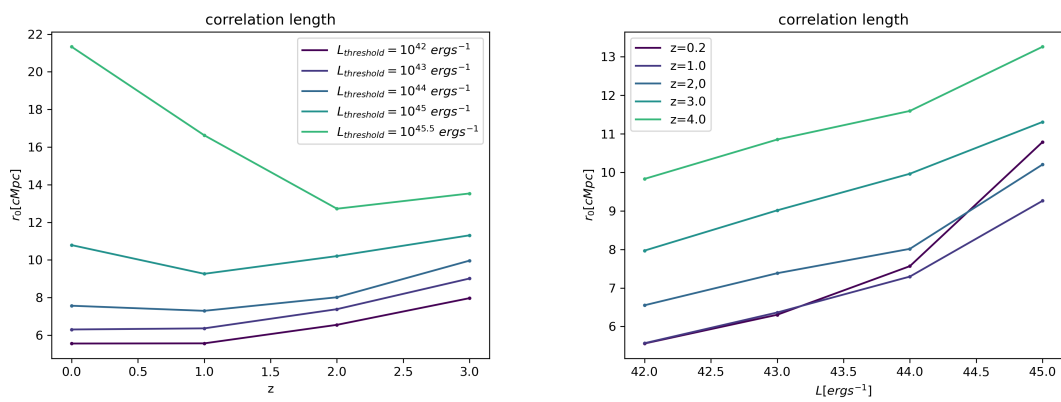


**Figure 5.8:** Left panel: The correlation length as a function of redshift, different colors represent different luminosity threshold. Right panel: The correlation length as a function of luminosity, different colors represent different redshift.

# 6 . Conclusion

Supermassive black holes are posited to reside at the centers of nearly all galaxies, with compelling evidence linking their formation to the evolutionary processes of galaxies. Quasars, which are intensely luminous active galactic nuclei (AGN), radiate extraordinarily strong emissions from their centers, primarily due to the accretion activities of supermassive black holes. By studying quasars, we can thus glean insights into black hole dynamics. In our work, utilizing data from the FLAMINGO simulation, we investigate the quasar luminosity function and quasar clustering within FLAMINGO. Following, we summarize our conclusions:

1. We analyzed the quasar luminosity function from the FLAMINGO simulation and compared it with observational data, observing a close match at redshift  $z = 0.2$ . However, at cosmic noon, the simulation underestimates the quantity of bright-end quasars. We identified two potential causes: the absence of super-Eddington ratios in the simulation of the black hole accretion processes, this limitation leads to an underestimation of the number of quasars at the bright-end of the QLFs. Another possible reason is that the evolutionary processes within galaxies where powerful radiation and jets expel gas, hindering star formation and causing massive black holes to become inactive. This enhances our understanding of galaxy evolution, suggesting a need for mechanisms that maintain black hole activity while quenching the galaxy.
2. Variations in the simulation, such as box size and resolution, were compared for their impact on the quasar luminosity functions (QLFs). We find that while box size has minimal influence, resolution significantly affects the outcomes, particularly at the faint end of QLFs, highlighting the importance of considering resolution in quasar studies. Furthermore, we investigated the effects of cosmological and astrophysical variations on QLFs, noting minimal impact from cosmological variations at low redshifts. Between  $z > 1.0$ , differences between HYDRO\_FIDUCIAL and HYDRO\_PLANCK were negligible, with HYDRO\_LOW\_SIGMA8 showing slightly fewer quasars. In terms of astrophysical simulations, different models showed minor impacts, with models with jet runs aligning more closely with observational data at the bright end.

- 
3. Decomposition of QLFs was conducted to examine their dominated components, focusing on Eddington ratios, black hole mass, and dark matter halo mass (in the Appendix A). The trend indicated that higher Eddington ratios and larger masses in black holes and dark matter halos dominate at higher luminosity segments. The decomposition of black hole mass highlighted the inactivity of supermassive black holes during the cosmic noon.
  4. Beyond studying the quasar luminosity function, we also explored the distribution of quasars in FLAMINGO through the projected correlation function. Analysis of different luminosity cuts showed that higher cuts correspond to stronger clustering, indicating that more luminous quasars tend to cluster more densely. The FLAMINGO simulation results matched observational data well at redshifts  $z = 0.2$  to  $3.0$ , but underestimated the correlation function at  $z = 4.0$ . Our work represents the first use of simulations to study quasar clustering for luminosity thresholds  $L > 10^{45} \text{ erg s}^{-1}$ .

# A . Appendix

## A.1 Eddington ratio distribution function

Figure A.1 shows the Eddington ratio distribution function in bins of the luminosity. Different colors represent different luminosity ranges.

## A.2 QLFs in bins of $M_{\text{dm}}$

Figure A.3 shows the decomposition of QLFs by the dark matter mass. We could find that higher luminosities correspond to higher dark matter mass. And we find at  $z = 0.2$  and  $z = 1.0$ ,  $10^{12} < M_{\text{dm}} < 10^{13} \text{ M}_{\odot}$  and  $10^{13} < M_{\text{BH}} < 10^{14} \text{ M}_{\odot}$  dominate the QLFs, especially the bright-end. At  $z > 1.0$ , the bright-ends of the QLFs are dominated by halos with  $10^{12} < M_{\text{dm}} < 10^{13} \text{ M}_{\odot}$ . This result is consistent with the DMH mass from clustering analysis in [Arita et al. \(2023\)](#). From Figure A.2, we find that most quasars reside in dark matter halos with masses  $10^{12} < M_{\text{dm}} < 10^{13} \text{ M}_{\odot}$ .

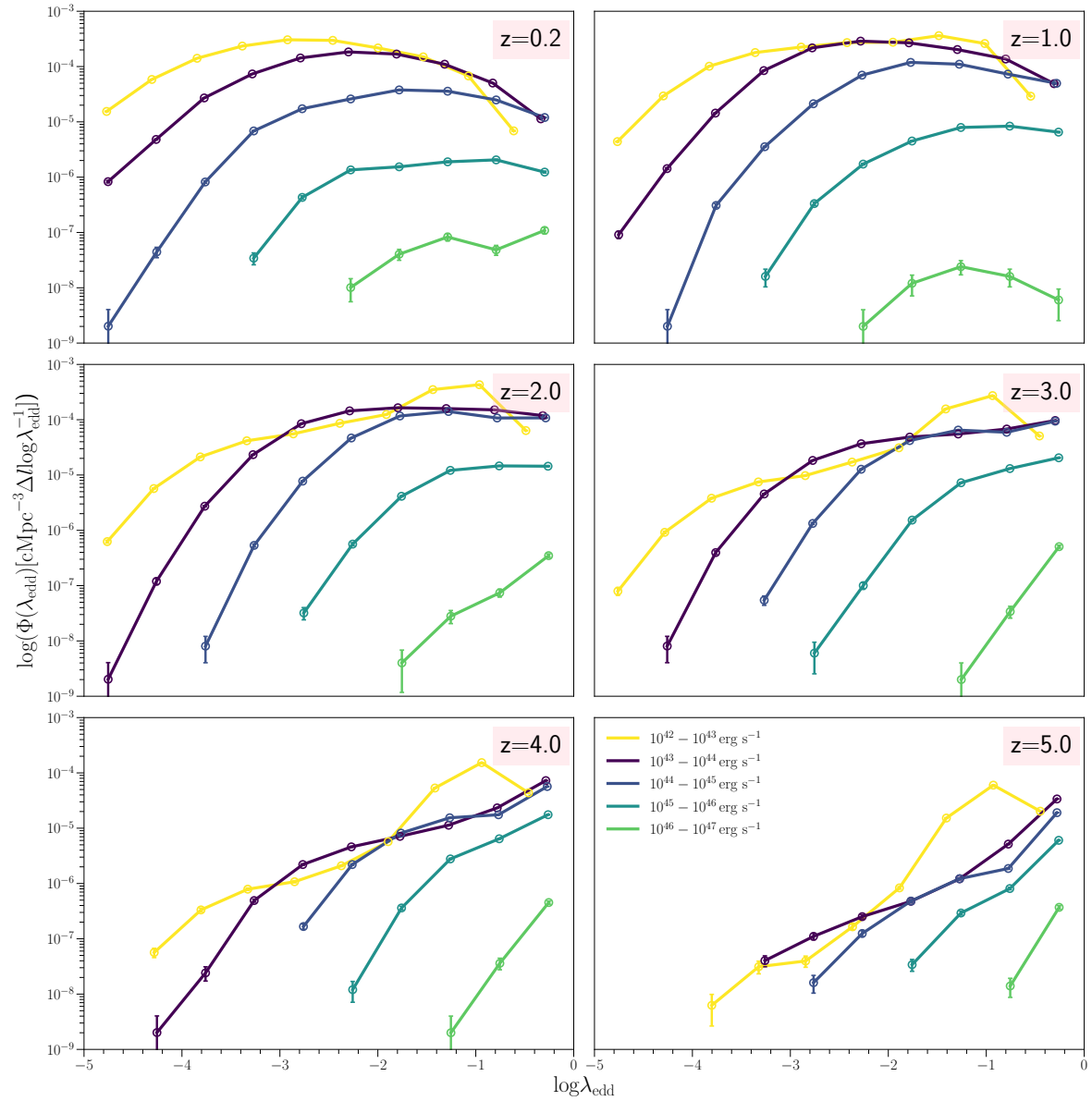


**Figure A.1:** Eddington ratio distribution function in bins of the luminosity. Different colors represent different luminosity ranges.

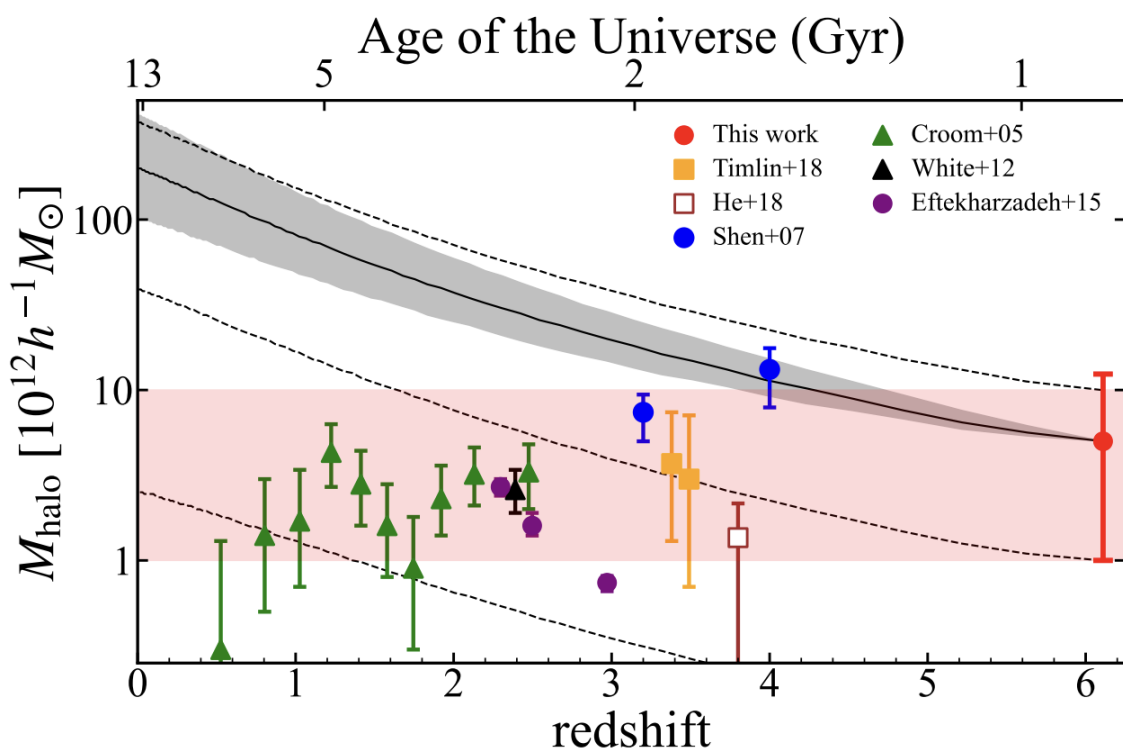


**Figure A.2:** The DMH mass from clustering analysis as a function of redshift. The references are shown in the upper right of the figure. The red-shaded region represents the DMH mass range where most of quasars are expected to reside. This plot is from [Arita et al. \(2023\)](#)

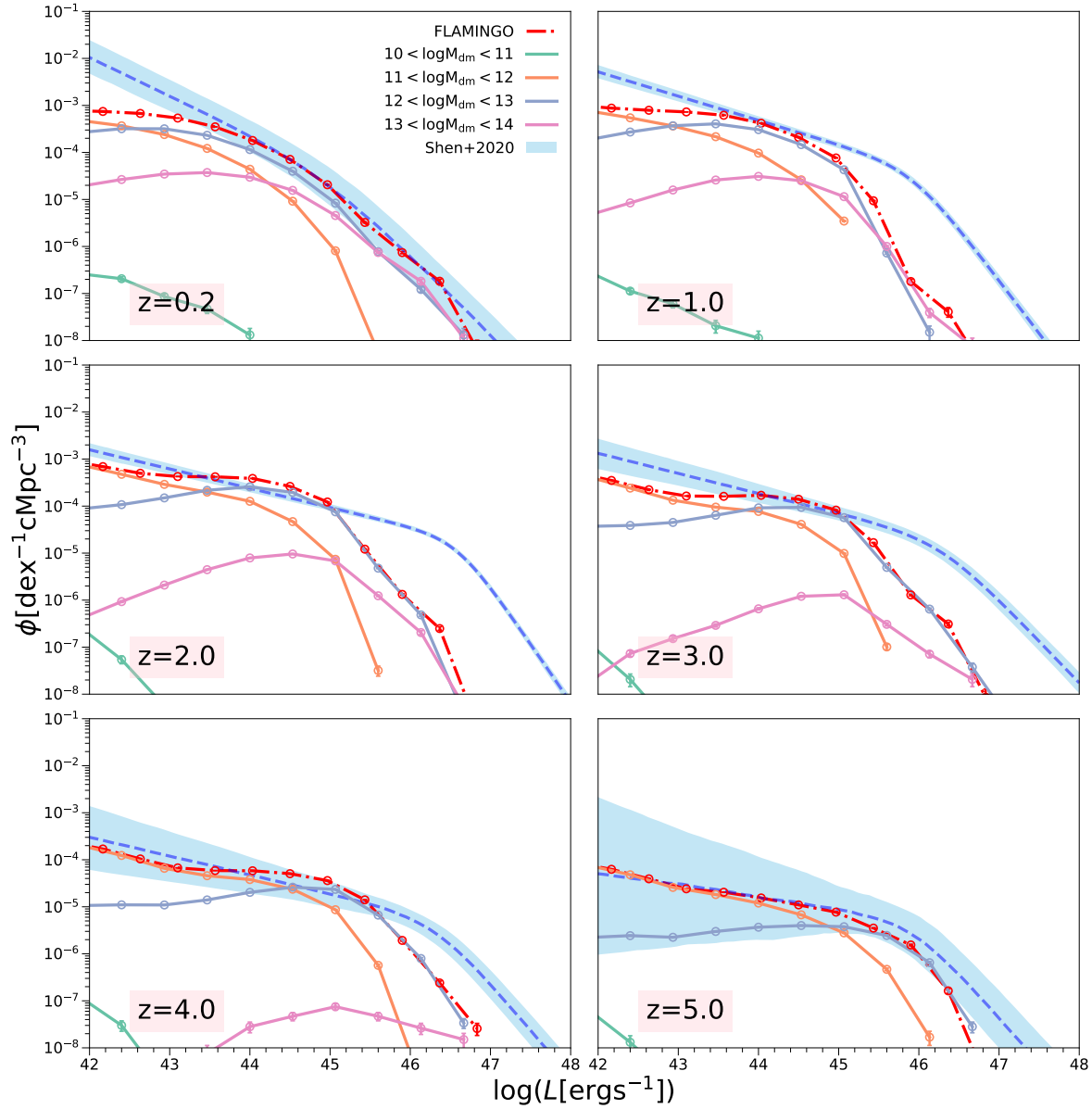


**Figure A.3:** Quasar luminosity functions in bins of the dark matter mass at  $z = 0.2$  (upper left),  $z = 1.0$  (upper right),  $z = 2.0$  (middle left),  $z = 3.0$  (middle right),  $z = 4.0$  (lower left), and  $z = 5.0$  (lower right). The red dashed-dotted lines represent the total QLFs. The solid colored lines are the decomposition of the QLFs. The shaded regions show the 68% confidence intervals from the fitting of the observational data.

# Bibliography

- Abbott, T., Aguena, M., Alarcon, A., et al. 2022, Physical Review D, 105, doi: [10.1103/physrevd.105.023520](https://doi.org/10.1103/physrevd.105.023520)
- Arita, J., Kashikawa, N., Matsuoka, Y., et al. 2023, ApJ , 954, 210, doi: [10.3847/1538-4357/ace43a](https://doi.org/10.3847/1538-4357/ace43a)
- Barger, A. J., Cowie, L. L., Mushotzky, R. F., et al. 2005, The Astronomical Journal, 129, 578–609, doi: [10.1086/426915](https://doi.org/10.1086/426915)
- Bañados, E., Venemans, B. P., Mazzucchelli, C., et al. 2017, Nature, 553, 473–476, doi: [10.1038/nature25180](https://doi.org/10.1038/nature25180)
- Behroozi, P., Wechsler, R. H., Hearin, A. P., & Conroy, C. 2019, MNRAS , 488, 3143, doi: [10.1093/mnras/stz1182](https://doi.org/10.1093/mnras/stz1182)
- Bondi, H., & Hoyle, F. 1944, MNRAS , 104, 273, doi: [10.1093/mnras/104.5.273](https://doi.org/10.1093/mnras/104.5.273)
- Bonoli, S., Marulli, F., Springel, V., et al. 2009, MNRAS , 396, 423, doi: [10.1111/j.1365-2966.2009.14701.x](https://doi.org/10.1111/j.1365-2966.2009.14701.x)
- Booth, C. M., & Schaye, J. 2009, Monthly Notices of the Royal Astronomical Society, 398, 53–74, doi: [10.1111/j.1365-2966.2009.15043.x](https://doi.org/10.1111/j.1365-2966.2009.15043.x)
- Borrow, J., Schaller, M., Bower, R. G., & Schaye, J. 2022, Monthly Notices of the Royal Astronomical Society, 511, 2367, doi: [10.1093/mnras/stab3166](https://doi.org/10.1093/mnras/stab3166)
- Boyle, B. J., Griffiths, R. E., Shanks, T., Stewart, G. C., & Georgantopoulos, I. 1993, MNRAS , 260, 49, doi: [10.1093/mnras/260.1.49](https://doi.org/10.1093/mnras/260.1.49)
- Boyle, B. J., Shanks, T., & Peterson, B. A. 1988, MNRAS , 235, 935, doi: [10.1093/mnras/235.3.935](https://doi.org/10.1093/mnras/235.3.935)
- Cowie, L. L., Songaila, A., Hu, E. M., & Cohen, J. G. 1996, AJ , 112, 839, doi: [10.1086/118058](https://doi.org/10.1086/118058)
- Crain, R. A., & van de Voort, F. 2023, Annual Review of Astronomy and Astrophysics, 61, 473–515, doi: [10.1146/annurev-astro-041923-043618](https://doi.org/10.1146/annurev-astro-041923-043618)

- Croton, D. J. 2009, Monthly Notices of the Royal Astronomical Society, 394, 1109–1119, doi: [10.1111/j.1365-2966.2009.14429.x](https://doi.org/10.1111/j.1365-2966.2009.14429.x)
- Degraf, C., Di Matteo, T., & Springel, V. 2010, Monthly Notices of the Royal Astronomical Society, 402, 1927–1936, doi: [10.1111/j.1365-2966.2009.16018.x](https://doi.org/10.1111/j.1365-2966.2009.16018.x)
- Di Matteo, T., Colberg, J., Springel, V., Hernquist, L., & Sijacki, D. 2008, The Astrophysical Journal, 676, 33–53, doi: [10.1086/524921](https://doi.org/10.1086/524921)
- Dubois, Y., Devriendt, J., Slyz, A., & Teyssier, R. 2012, Monthly Notices of the Royal Astronomical Society, 420, 2662–2683, doi: [10.1111/j.1365-2966.2011.20236.x](https://doi.org/10.1111/j.1365-2966.2011.20236.x)
- Efstathiou, G., Davis, M., White, S. D. M., & Frenk, C. S. 1985, ApJS, 57, 241, doi: [10.1086/191003](https://doi.org/10.1086/191003)
- Eftekhari-zadeh, S., Myers, A. D., White, M., et al. 2015, Monthly Notices of the Royal Astronomical Society, 453, 2780–2799, doi: [10.1093/mnras/stv1763](https://doi.org/10.1093/mnras/stv1763)
- Elahi, P. J., Cañas, R., Poulton, R. J. J., et al. 2019, Publications of the Astronomical Society of Australia, 36, doi: [10.1017/pasa.2019.12](https://doi.org/10.1017/pasa.2019.12)
- Elbers, W., Frenk, C. S., Jenkins, A., Li, B., & Pascoli, S. 2021, Monthly Notices of the Royal Astronomical Society, 507, 2614, doi: [10.1093/mnras/stab2260](https://doi.org/10.1093/mnras/stab2260)
- . 2022, Monthly Notices of the Royal Astronomical Society, 516, 3821, doi: [10.1093/mnras/stac2365](https://doi.org/10.1093/mnras/stac2365)
- Ferrarese, L., & Merritt, D. 2000, ApJL, 539, L9, doi: [10.1086/312838](https://doi.org/10.1086/312838)
- Gebhardt, K., Bender, R., Bower, G., et al. 2000, ApJL, 539, L13, doi: [10.1086/312840](https://doi.org/10.1086/312840)
- Gültekin, K., Richstone, D. O., Gebhardt, K., et al. 2009, ApJ, 698, 198, doi: [10.1088/0004-637X/698/1/198](https://doi.org/10.1088/0004-637X/698/1/198)
- Hahn, O., Rampf, C., & Uhlemann, C. 2021, Monthly Notices of the Royal Astronomical Society, 503, 426, doi: [10.1093/mnras/staa3773](https://doi.org/10.1093/mnras/staa3773)
- Hazard, C., Mackey, M. B., & Shimmins, A. J. 1963, Nature, 197, 1037, doi: [10.1038/1971037a0](https://doi.org/10.1038/1971037a0)
- Hopkins, P. F., Hernquist, L., Cox, T. J., et al. 2005, ApJ, 630, 705, doi: [10.1086/432438](https://doi.org/10.1086/432438)
- . 2006, ApJS, 163, 1, doi: [10.1086/499298](https://doi.org/10.1086/499298)
- Kormendy, J., & Richstone, D. 1995, ARA&A, 33, 581, doi: [10.1146/annurev.aa.33.090195.003053](https://doi.org/10.1146/annurev.aa.33.090195.003053)

- Kugel, R., Schaye, J., Schaller, M., et al. 2023, MNRAS , 526, 6103, doi: [10.1093/mnras/stad2540](https://doi.org/10.1093/mnras/stad2540)
- La Franca, F., Andreani, P., & Cristiani, S. 1998, ApJ , 497, 529, doi: [10.1086/305508](https://doi.org/10.1086/305508)
- Lidz, A., Hopkins, P. F., Cox, T. J., Hernquist, L., & Robertson, B. 2006, The Astrophysical Journal, 641, 41–49, doi: [10.1086/500444](https://doi.org/10.1086/500444)
- Matthews, T. A., & Sandage, A. R. 1963, ApJ , 138, 30, doi: [10.1086/147615](https://doi.org/10.1086/147615)
- Matute, I., La Franca, F., Pozzi, F., et al. 2006, A&A , 451, 443, doi: [10.1051/0004-6361:20053710](https://doi.org/10.1051/0004-6361:20053710)
- Mortlock, D. J., Warren, S. J., Venemans, B. P., et al. 2011, Nature, 474, 616–619, doi: [10.1038/nature10159](https://doi.org/10.1038/nature10159)
- Schaller, M., Borrow, J., Draper, P. W., et al. 2023, Swift: A modern highly-parallel gravity and smoothed particle hydrodynamics solver for astrophysical and cosmological applications, arXiv. <http://arxiv.org/abs/2305.13380>
- Schaye, J., Kugel, R., Schaller, M., et al. 2023, MNRAS , 526, 4978, doi: [10.1093/mnras/stad2419](https://doi.org/10.1093/mnras/stad2419)
- Schmidt, M. 1963, Nature , 197, 1040, doi: [10.1038/1971040a0](https://doi.org/10.1038/1971040a0)
- . 1968, ApJ , 151, 393, doi: [10.1086/149446](https://doi.org/10.1086/149446)
- Schmidt, M., & Green, R. F. 1983, ApJ , 269, 352, doi: [10.1086/161048](https://doi.org/10.1086/161048)
- Shen, X., Hopkins, P. F., Faucher-Giguère, C.-A., et al. 2020, Monthly Notices of the Royal Astronomical Society, 495, 3252–3275, doi: [10.1093/mnras/staa1381](https://doi.org/10.1093/mnras/staa1381)
- Shen, Y., Strauss, M. A., Oguri, M., et al. 2007, AJ , 133, 2222, doi: [10.1086/513517](https://doi.org/10.1086/513517)
- Shen, Y., Strauss, M. A., Ross, N. P., et al. 2009, The Astrophysical Journal, 697, 1656–1673, doi: [10.1088/0004-637x/697/2/1656](https://doi.org/10.1088/0004-637x/697/2/1656)
- Springel, V., White, S. D. M., Jenkins, A., et al. 2005, Nature , 435, 629, doi: [10.1038/nature03597](https://doi.org/10.1038/nature03597)
- Ueda, Y., Akiyama, M., Ohta, K., & Miyaji, T. 2003, ApJ , 598, 886, doi: [10.1086/378940](https://doi.org/10.1086/378940)
- Venemans, B. P., Verdoes Kleijn, G. A., Mwebaze, J., et al. 2015, Monthly Notices of the Royal Astronomical Society, 453, 2260–2267, doi: [10.1093/mnras/stv1774](https://doi.org/10.1093/mnras/stv1774)
- Vogelsberger, M., Marinacci, F., Torrey, P., & Puchwein, E. 2019, Cosmological Simulations of Galaxy Formation. <https://arxiv.org/abs/1909.07976>
- Webster, B. L., & Murdin, P. 1972, Nature , 235, 37, doi: [10.1038/235037a0](https://doi.org/10.1038/235037a0)